










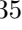


Quasi-periodic X-ray eruptions years after a nearby tidal disruption event

M. Nicholl¹, D. R. Pasham², A. Mummery³, M. Guolo⁴,
 K. Gendreau⁵, G. C. Dewangan⁶, E. C. Ferrara^{7,8,5}, R. Remillard²,
 C. Bonnerot^{9,10}, J. Chakraborty², A. Hajela¹¹, V. S. Dhillon^{12,13}, A. F. Gillan¹,
 J. Greenwood¹, M. E. Huber¹⁴, A. Janiuk¹⁵, G. Salvesen¹⁶, S. van Velzen¹⁷,
 A. Aamer¹, K. D. Alexander¹⁸, C. R. Angus¹, Z. Arzoumanian⁵, K. Auchettl^{19,20},
 E. Berger²¹, T. de Boer¹⁴, Y. Cendes^{21,22}, K. C. Chambers¹⁴, T.-W. Chen²³,
 R. Chornock²⁴, M. D. Fulton¹, H. Gao¹⁴, J. H. Gillanders²⁵, S. Gomez²⁶,
 B. P. Gompertz^{9,10}, A. C. Fabian²⁷, J. Herman¹⁴, A. Ingram²⁸, E. Kara²,
 T. Laskar^{29,30}, A. Lawrence³¹, C.-C. Lin¹⁴, T. B. Lowe¹⁴, E. A. Magnier¹⁴,
 R. Margutti²⁴, S. L. McGee^{9,10}, P. Minguez¹⁴, T. Moore¹, E. Nathan³²,
 S. R. Oates³³, K. C. Patra²⁴, P. Ramsden^{1,9,10}, V. Ravi³², E. J. Ridley^{9,10},
 X. Sheng¹, S. J. Smartt^{25,1}, K. W. Smith¹, S. Srivastav^{25,1}, R. Stein³⁴,
 H. F. Stevance^{25,1}, S. G. D. Turner³⁵, R. J. Wainscoat¹⁴,
 J. Weston¹, T. Wevers²⁶, D. R. Young¹

¹Astrophysics Research Centre, School of Mathematics and Physics, Queens University Belfast,
 Belfast BT7 1NN, UK

²Kavli Institute for Astrophysics and Space Research, Massachusetts Institute of Technology,
 Cambridge, MA, USA

³Oxford Theoretical Physics, Beecroft Building, Clarendon Laboratory, Parks Road, Oxford,
 OX1 3PU, UK

⁴Department of Physics and Astronomy, Johns Hopkins University, 3400 N. Charles St.,
 Baltimore MD 21218, USA

⁵NASA Goddard Space Flight Center, Code 662, Greenbelt, MD 20771, USA

- ⁶Inter-University Centre for Astronomy and Astrophysics (IUCAA), PB No.4, Ganeshkhind,
Pune-411007, India
- ⁷Department of Astronomy, University of Maryland, College Park, MD, 20742, USA
- ⁸Center for Research and Exploration in Space Science & Technology II (CRESST II),
NASA/GSFC, Greenbelt, MD 20771, USA
- ⁹School of Physics and Astronomy, University of Birmingham, Birmingham B15 2TT
- ¹⁰Institute for Gravitational Wave Astronomy, University of Birmingham, Birmingham
B15 2TT
- ¹¹DARK, Niels Bohr Institute, University of Copenhagen, Jagtvej 155, 2200 Copenhagen,
Denmark
- ¹²Department of Physics and Astronomy, University of Sheffield, Sheffield, S3 7RH,
United Kingdom
- ¹³ Instituto de Astrofísica de Canarias, E-38205 La Laguna, Tenerife, Spain
- ¹⁴Institute for Astronomy, University of Hawaii, 2680 Woodlawn Drive, Honolulu HI
96822, USA
- ¹⁵Center for Theoretical Physics, Polish Academy of Sciences, Al. Lotnikow 32/46,
02-668, Warsaw, Poland
- ¹⁶Center for Theoretical Astrophysics, Los Alamos National Laboratory, Los Alamos,
NM 87545, USA
- ¹⁷Leiden Observatory, Leiden University,
Postbus 9513, 2300 RA Leiden, The Netherlands
- ¹⁸Department of Astronomy and Steward Observatory, University of Arizona, 933 North
Cherry Avenue, Tucson, AZ 85721-0065, USA
- ¹⁹School of Physics, The University of Melbourne, VIC 3010, Australia
- ²⁰Department of Astronomy and Astrophysics, University of California, Santa Cruz,
CA 95064, USA
- ²¹Center for Astrophysics, Harvard & Smithsonian, 60 Garden Street, Cambridge,
MA 02138-1516, USA
- ²²Department of Physics, University of Oregon, Eugene, OR 97403, USA
- ²³Graduate Institute of Astronomy, National Central University, 300 Jhongda Road,
32001 Jhongli, Taiwan
- ²⁴Department of Astronomy, University of California, Berkeley, CA 94720-3411, USA
- ²⁵Astrophysics sub-Department, Department of Physics, University of Oxford, Keble Road,
Oxford, OX1 3RH, UK

²⁶Space Telescope Science Institute, 3700 San Martin Drive, Baltimore, MD 21218, USA

²⁷Institute of Astronomy, University of Cambridge, Madingley Road, Cambridge
CB3 0HA, UK

²⁸School of Mathematics, Statistics and Physics, Newcastle University, Herschel Building,
Newcastle upon Tyne, NE1 7RU, UK

²⁹Department of Physics & Astronomy, University of Utah, Salt Lake City, UT 84112, USA

³⁰Department of Astrophysics/IMAPP, Radboud University, P.O. Box 9010, 6500 GL,
Nijmegen, The Netherlands

³¹Institute for Astronomy, University of Edinburgh, Royal Observatory, Blackford Hill,
Edinburgh EH9 3HJ, UK

³²Cahill Center for Astronomy and Astrophysics, California Institute of Technology,
Pasadena, CA 91125, USA

³³Department of Physics, Lancaster University, Lancaster LA1 4YB, UK

³⁴Division of Physics, Mathematics, and Astronomy, California Institute of Technology,
Pasadena, CA 91125, USA

³⁵Department of Applied Mathematics and Theoretical Physics, University of
Cambridge, Wilberforce Road, Cambridge, CB3 0WA, UK

September 5, 2024

Quasi-periodic Eruptions (QPEs) are luminous bursts of soft X-rays from the nuclei of galaxies, repeating on timescales of hours to weeks [1, 2, 3, 4, 5]. The mechanism behind these rare systems is uncertain, but most theories involve accretion disks around supermassive black holes (SMBHs), undergoing instabilities [6, 7, 8] or interacting with a stellar object in a close orbit [9, 10, 11]. It has been suggested that this disk could be created when the SMBH disrupts a passing star [11, 8], implying that many QPEs should be preceded by observable tidal disruption events (TDEs). Two known QPE sources show long-term decays in quiescent luminosity consistent with TDEs [12, 4], and two observed TDEs have exhibited X-ray flares consistent with individual eruptions [13, 14].

TDEs and QPEs also occur preferentially in similar galaxies [15]. However, no confirmed repeating QPEs have been associated with a spectroscopically confirmed TDE or an optical TDE observed at peak brightness. Here we report the detection of nine X-ray QPEs with a mean recurrence time of approximately 48 hours from AT2019qiz, a nearby and extensively studied optically-selected TDE [16]. We detect and model the X-ray, ultraviolet and optical emission from the accretion disk, and show that an orbiting body colliding with this disk provides a plausible explanation for the QPEs.

The TDE AT2019qiz was discovered by the Zwicky Transient Facility (ZTF) on 2019-09-19 UT (Universal Time), at Right Ascension 04:46:37.88 and Declination -10:13:34.90 (J2000.0 epoch), in the nucleus of a barred spiral galaxy at redshift $z = 0.0151$ (luminosity distance of 65.6 Mpc). Its optical spectrum was typical of TDEs, with broad emission lines from hydrogen and ionised helium [16], and it is a particularly well-studied event due to its proximity and early detection [16, 17, 18]. The ultraviolet (UV) and optical luminosity declined over a few months until reaching a steady, years-long plateau at $\sim 10^{41}$ erg s $^{-1}$ [19], consistent with an exposed accretion disk [20, 19]. Highly ionized iron lines appeared at this phase, indicating a gas-rich environment ionized by the TDE [21]. The mass of the central SMBH has been estimated as a few $\times 10^6 M_{\odot}$ (where M_{\odot} is the solar mass) using various techniques (Extended Data Table 1).

We observed AT2019qiz on 2023-12-09 and 2023-12-10 UT (approximately 1500 days after its first optical detection) with the *Chandra* X-ray observatory and on 2023-12-21 UT with the *Hubble Space Telescope (HST)* as part of a joint program to study TDE accretion disks. The *Chandra* data were obtained across three exposures of 15.4, 18.8 and 16.1 ks, shown in Fig. 1a. The average count rate in the *Chandra* broad band (0.5 – 7 keV) is more than an order of magnitude larger in the middle exposure than in the first and final exposures. The *Chandra* images show another X-ray source ≈ 7 arcseconds south-east (SE) of AT2019qiz, but the high spatial resolution of the *Chandra* images (~ 0.5 arcseconds) allows us to definitively associate

the increase in count rate with AT2019qiz. The count rate increases and then decreases over the course of the middle exposure, while no other source in the field (Extended Data Fig. 1) shows evidence for variability. By analysing the spectra of these sources, we find that reported X-rays from *Swift*/XRT during the initial optical flare in 2019-2020 [16] are instead detections of the nearby SE source, and we exclude these from any analysis in this work (Methods).

To probe the variability of AT2019qiz further, we obtained high-cadence observations using the Neutron Star Interior Composition Explorer (*NICER*) from 2024-02-29 to 2024-03-09 UT, the X-ray Telescope (XRT) on-board the Neil Gehrels *Swift* Observatory on 2024-03-12 UT, and *AstroSat* starting on 2024-03-14 UT. The soft X-ray (0.3-1.0 keV) light curves from *NICER* showed repeating sharp increases in count rate followed by a return to quiescence, with six consecutive peaks detected in just over 10 days. Two more peaks were detected over the next four days with *Swift*/XRT and *AstroSat*. The light curves are shown in Fig. 1b. The time between successive peaks ranges from 39 to 54 hours in the rest-frame, measured by fitting skewed Gaussian profiles (Extended Data Fig. 2). The mean recurrence time is 48.4 ± 0.3 hours, with a standard deviation of 7.2 hours. Typical durations are 8–10 hours, with a consistent light curve shape exhibiting a fast rise and slower decay (Fig. 1c).

The combination of soft X-ray sensitivity and cadence in the *NICER* data allows us to perform time-resolved spectral fitting (Fig. 2, Extended Data Fig. 3). The nearby SE source detected by *Chandra* does not contribute significantly in the *NICER* bandpass (Methods). Single-temperature blackbody fits to the second *NICER* peak (chosen for good temporal coverage and low background; Methods) show an increasing temperature as the luminosity rises, and a lower temperature for the same luminosity during the decay phase, due to an increase in the blackbody radius. The expanding emitting region is ~ 1 solar radius ($\sim 10^{11}$ cm). The bolometric luminosity at peak reaches $(1.8 \pm 0.1) \times 10^{43}$ erg s $^{-1}$, with a temperature of 109 ± 1 eV. In the quiescent phase, spectral information could only be retrieved by stacking the data from *Swift*/XRT. This can be well modeled as a color-corrected disk model with maximum disk temperature

$kT_p \approx 67 \pm 10$ eV (Methods, Extended Data Fig. 4).

All of the above properties are consistent with the six known QPE sources repeating on timescales of hours to days [1, 2, 3, 4] and the longer duration Swift J0230+28 [5, 22]. This includes the luminosity and temperature, both in eruption and quiescence, and the lack of any detected optical/UV variability (Extended Data Fig. 5). The ‘hysteresis loop’ in the luminosity-temperature plane (Fig. 2c) is characteristic of QPE emission [23, 12, 24]. The recurrence time and eruption duration are towards the higher ends of their respective distributions (though well below Swift J0230+28), but their ratio of ≈ 0.2 is consistent with the duty cycle of 0.24 ± 0.13 exhibited by other QPEs [5] (Fig. 3). Performing our own correlation analysis on duration versus recurrence time for the QPE population including AT2019qiz yields strong Bayesian evidence in favour of a correlation, with a mean duty cycle of $0.22^{+0.11}_{-0.04}$ (Methods). The $\approx 15\%$ variation in recurrence times in AT2019qiz is also similar to known QPEs. The variations in AT2019qiz appear somewhat irregular, but with a limited number of cycles we cannot establish robustly at this point whether or not there is an underlying pattern of alternating long and short recurrence times, as seen in some of the other QPE sources [1, 3].

We conclude that AT2019qiz is now exhibiting X-ray QPEs fully consistent with the known source population, and with an average recurrence time $T_{\text{QPE}} \approx 48$ hours. Our result confirms theoretical predictions that at least some QPEs arise in accretion disks created by TDEs [8, 11] (although we note that QPEs have also been discovered in galaxies with evidence for active nuclei [15]). It also increases confidence in the candidate QPEs following the TDEs AT2019vcb [14] and XMMSL1 J0249 [13], and the proposed X-ray TDE in the QPE source GSN 069 [12]. We are unable to constrain when QPEs began in AT2019qiz, though *NICER* data in the two months around optical peak exhibit no QPEs. XRT data obtained on 2022-01-13 (~ 840 days after disruption) over a duration of 25 hours show the possible beginning of an eruption, but the duration of the observation is too short to confirm this (Methods; Extended Data Fig. 6).

Our *HST* imaging shows UV emission (effective wavelength 2357 Å) coincident with the

nucleus of the host galaxy. At this distance the luminosity is $\nu L_\nu = 3.2 \times 10^{41} \text{ erg s}^{-1}$. This source is unresolved, indicating an angular size $\lesssim 0.08$ arcseconds or 25 pc (Extended Data Fig. 7). The luminosity is consistent with a TDE accretion disk [20], but not with a nuclear star cluster (Methods). We also detect far-UV emission (1480 Å) with *AstroSat*. We model the UV and quiescent X-ray light curves, alongside 3.5 years of optical measurements from the Panoramic Survey Telescope and Rapid Response System (Pan-STARRS) and ZTF, using a time-dependent relativistic thin disk [25] (Fig. 4, Methods). We find a SMBH mass $\log_{10} M_\bullet/M_\odot = 6.3_{-0.2}^{+0.3}$, and an initial disk mass $M_{\text{disk}}/M_\odot = 0.06_{-0.03}^{+0.04}$ (Extended Data Fig. 8).

The properties of the disk help to constrain the cause of the QPE emission. In models of disk pressure instability, the variability amplitude and recurrence timescale depend on the SMBH mass and accretion rate. With the SMBH mass well constrained, the late-time disk luminosity is $(4 \pm 1)\%$ of the Eddington luminosity. At this Eddington ratio, radiation pressure instability models can explain the amplitude of the eruptions, but predict a recurrence time of \sim years [26]. A disk that is dominated by magnetic (rather than radiation) pressure is expected to be stable for this mass and Eddington ratio [8]. We therefore examine models that can explain QPE emission on hour-day timescales within a stable disk. These models involve another body (a star or compact object) already on a close, decaying orbit around the SMBH (an extreme mass-ratio inspiral, or EMRI), that interacts with the spreading disk from the TDE once the disk is sufficiently radially extended.

The disk size is well constrained in our analysis by the UV and optical emission (Fig. 4), and is several times larger than an orbit with a 48.4 hour period (radius $\approx 200GM_\bullet/c^2$). Since any orbiting body with this period is expected to cross the disk, this provides a promising explanation for the observed QPEs. The same argument applies also to a 98.6 hour orbit, required if interactions occur twice per orbit (Fig. 4). The luminosity in this model can be produced by the ejection of shocked disk material [11], shock breakout within the disk [27], or a temporarily enhanced accretion rate [28]. The compact emitting radius and its expansion during the erup-

tions may favour the first of these mechanisms. As the density of expanding ejecta decreases, we would expect the photosphere (the surface of the optically thick region) eventually to recede, consistent with our findings in Fig. 2d.

In the simplest case of an EMRI crossing the disk twice per elliptical orbit, recurrence times would exhibit an alternating long-short pattern, as seen in a subset of the known QPE sources [1, 3]. In the EMRI model, more complex timing behaviour [2, 23] can be caused by relativistic precession of the disk if its rotational axis is misaligned with that of the SMBH [29, 10, 30]. Significant precession over the course of a few cycles in AT2019qiz would require a dimensionless SMBH spin $a_{\bullet} \gtrsim 0.5 - 0.7$; however, such a large spin would tend to align the disk and damp precession in $\ll 1000$ days (Methods). Changing gas dynamics following star-disk collisions has recently been proposed as an alternative way to explain QPE timing variations [31]. Continuing high-cadence observations of AT2019qiz will be required to better constrain the nature of its timing variations and enable more detailed comparisons to QPE models.

The serendipitous discovery of QPEs in TDE AT2019qiz suggests that QPEs following TDEs may be common. We find that the long-term accretion disk properties in AT2019qiz are consistent with the star-disk interaction model for QPEs, indicating that the fraction of TDEs with QPEs can be used to constrain the rate of EMRIs, an important goal for future gravitational wave detectors [32]. The latest observational estimates of the QPE rate [24] are about one-tenth of the TDE rate [33, 34], consistent with recent theoretical predictions for the formation rate and lifetimes of EMRIs [35]. The QPEs in AT2019qiz show that long-term, high-cadence X-ray follow-up of optical TDEs will be a powerful tool for future QPE discovery, without the need for wide-field X-ray time-domain surveys, providing a path to measure the EMRI rate directly through electromagnetic observations.

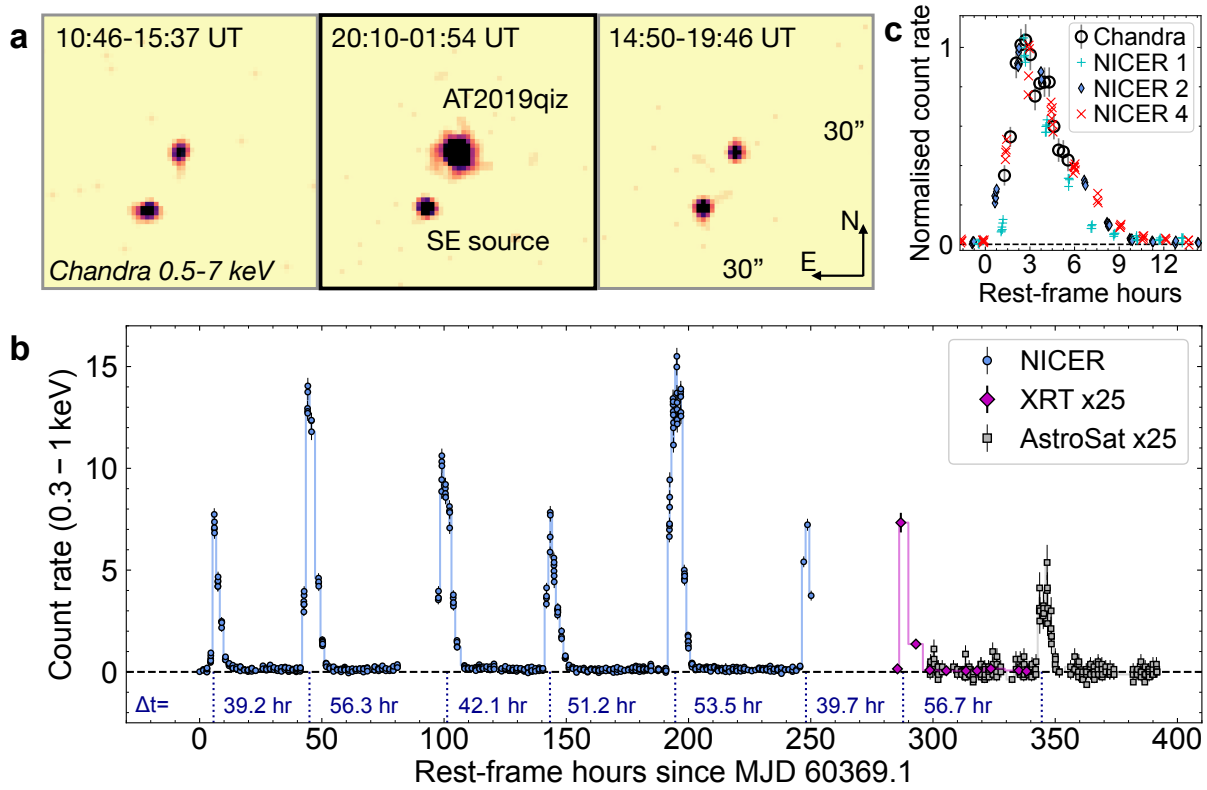


Figure 1: **Detection of QPEs from the nearby TDE AT2019qiz.** (a) *Chandra* images obtained from exposures on 2023-12-09 and 2023-12-10. Observation times are shown in UT. Each image shows a 30 by 30 arcsecond region centered on AT2019qiz. Images have been smoothed with a 2 pixel Gaussian filter for clarity. The nearby source to the south-east shows a consistent flux across the three exposures. (b) Light curve showing eight eruptions detected by *NICER*, *Swift*/XRT and *AstroSat* from 2024-02-29 to 2024-03-14 (MJD 60369 – 60383). Without stacking, the count rate between the eruptions is consistent with zero. Time delays between eruptions are labelled. The mean (standard deviation) recurrence time is 48.4 (7.2) hours. (c) Comparison of light curve shapes between the *Chandra* eruption from December 2023 and *NICER* eruptions from March 2024. The fast rise and shallower decay remains consistent over several months. All error bars show 1σ uncertainties.

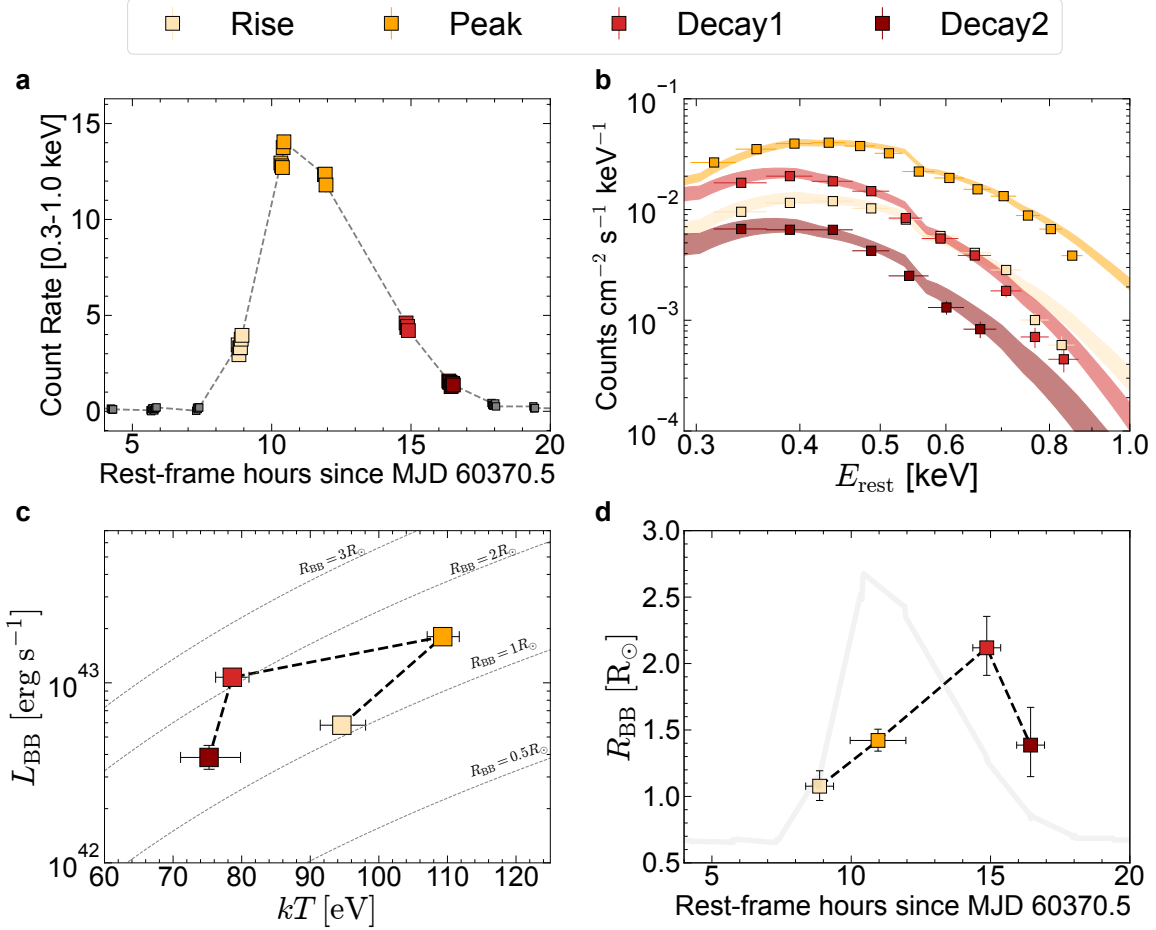


Figure 2: **NICER time-resolved spectroscopy of the second eruption in Fig. 1b.** (a) Light curve of the eruption, with the rise, peak and decay phases indicated by the colour-coding. (b) Fits to the spectrum during each phase, using a single-temperature blackbody model (Methods). The shaded regions are 90% confidence intervals. (c) Blackbody luminosity plotted against temperature for each fit. The eruption shows an anti-clockwise ‘hysteresis’ cycle in this parameter space. Error bars show the 90% confidence regions of the model posteriors. (d) Blackbody radius against time, overlaid on eruption light curve (grey). The blackbody radius increases during the eruption, with a maximum radius at the decay. We see tentative evidence in the final bin for contraction of the photosphere, which can be explained if the density and thus optical depth decrease as material expands.

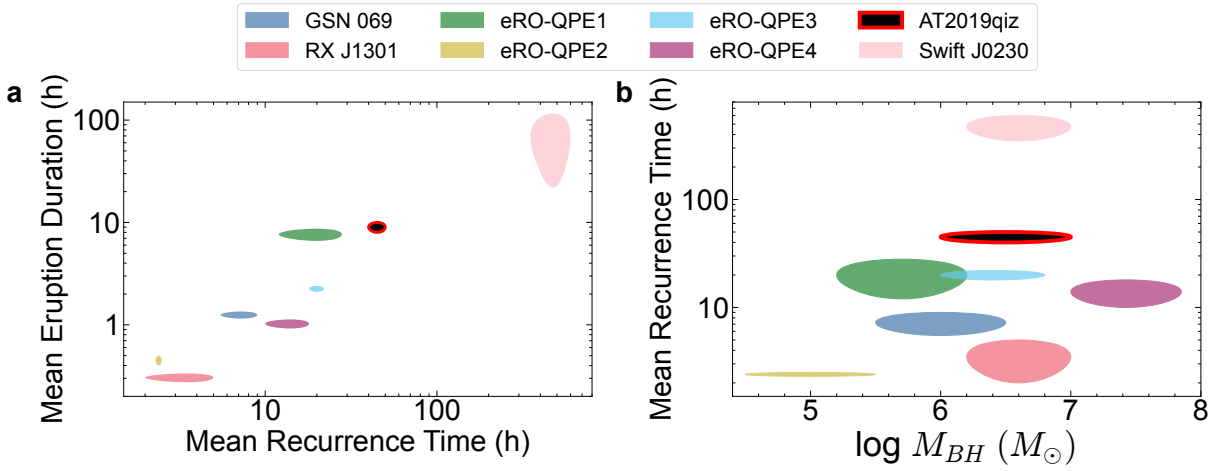


Figure 3: **Eruption properties in AT2019qiz compared to the other known QPE sources.** (a) Mean eruption duration vs mean recurrence time. QPEs exhibit a clear correlation, with broader eruptions occurring for systems with longer recurrence times. The known QPE sources spend $24 \pm 13\%$ of their time in outburst [5]. AT2019qiz is consistent with this trend. (b) Mean recurrence time vs reported SMBH mass from host galaxy scaling relations [16, 5]. AT2019qiz is completely typical of the known QPE population in terms of its SMBH mass, and supports previous findings [5] that recurrence times in QPEs are not correlated with SMBH mass. The shaded regions represent the observed ranges of durations and recurrence times, while for the SMBH masses they represent the 1σ uncertainty from scaling relations used to derive the masses [5].

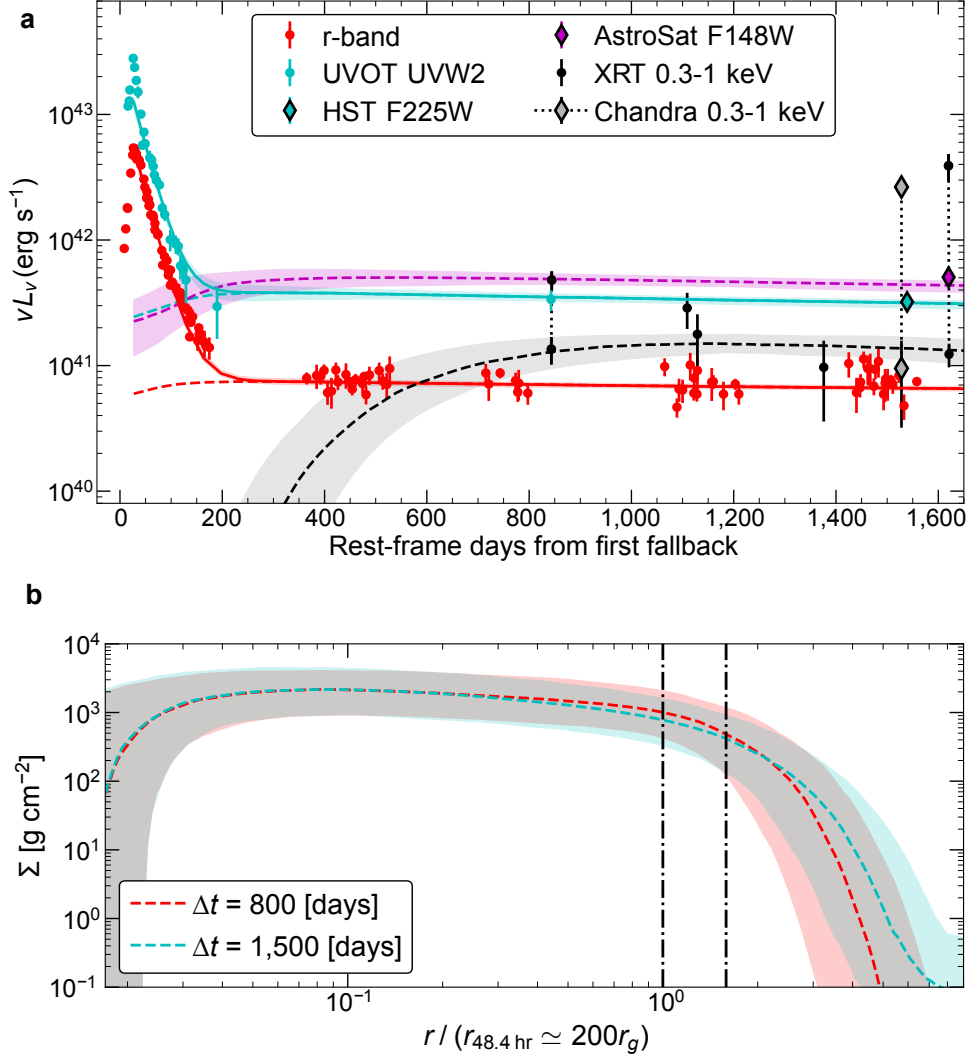


Figure 4: **Multi-wavelength light curves with disk model fit.** (a) X-ray, UV and optical data showing the TDE in 2019 [16] and the long-term disk emission. The dashed lines and shaded regions show the median and 90% confidence range of our accretion disk model fit [25]. QPEs (dotted lines) were excluded from the fit. A potential earlier QPE is also seen in X-ray data at ~ 800 days [21]. Our model is agnostic to the mechanism powering the initial UV/optical peak (Methods), but by the time of the QPEs all data are consistent with an exposed accretion disk. (b) Radial surface density profiles of the best-fit model at 800 and 1500 days after disruption (including 90% confidence range). The radius has been normalised to the circular orbit with period $T_{\text{orb}} = T_{\text{QPE}}$. The vertical lines indicate the orbital radii corresponding to periods of $1 \times$ and $2 \times T_{\text{QPE}}$. Both orbits cross the disk plane, showing that star-disk interactions occurring either once or twice per orbit can explain the QPEs in AT2019qiz [11].

Methods

1 Observations and Data Analysis

1.1 X-ray data

1.1.1 *Chandra*

We downloaded processed *Chandra* images and event files and associated calibration data from the *Chandra* archive. Analysis was performed using CIAO (version 4.16) [36] and CALBD version 4.11.0. We checked for pileup using the PILEUP_MAP task, finding a pileup fraction of $\approx 1\%$ only for the central 4 pixels of the middle exposure. Therefore pileup has negligible impact on our analysis. Count rates were extracted using the SRCFLUX task. We used a 2 arcsecond (4 pixel) circular radius and the default PSF model. The background was estimated using an annular region with inner and outer radii of 15 and 60 arcseconds centered on AT2019qiz. This excludes other point sources including the south-east source (see below). The CIAO SRCFLUX task includes the Bayesian Gregory-Loredo (G-L) algorithm [37] to determine the optimal number of bins for investigating a time-varying (or more formally, periodic) signal. The algorithm provides an odds ratio for variability (2.5 for AT2019qiz) and a light curve with the number of bins that maximises this odds ratio. None of the other five sources in Extended Data Fig. 1 show an odds ratio > 1 .

We extract the spectrum both in eruption and quiescence (see below) using the SPEXTRACT task. The spectrum of the eruption is soft, and can be reasonably fit with a blackbody of ≈ 100 eV. We perform a more detailed spectral analysis of AT2019qiz using the later eruptions and quiescent-phase data from instruments with greater sensitivity to softer (0.3-0.7 keV) X-rays (sections 1.1.3, 1.1.5).

1.1.2 The nature of the SE X-ray source

The *Chandra* images show a nearby source ≈ 7 arcsecs to the southeast (labeled ‘SE source’; Fig. 1). It overlaps with the point-spread function of AT2019qiz in all instruments other than *Chandra*. We extracted individual X-ray (0.5 – 7.0 keV) spectra from all three *Chandra* obsIDs to characterize the SE source. We perform spectral analysis with the Bayesian X-ray Analysis software (BXA) version 4.0.7 [38], which connects the nested sampling algorithm UltraNest [39] with the fitting environment XSPEC version 12.13.0c [40], in its Python version PYXSPEC. To improve the quality of the spectrum, we jointly fit all 3 *Chandra* obsIDs. The source can be fit with a simple power-law model with foreground absorption (TBABS×CFLUX(POW)) and is consistent with being constant over all three obsIDs. The neutral column density was fixed at the Milky Way value of $6.6 \times 10^{20} \text{ cm}^{-2}$. The 0.5 – 3.0 keV flux in the model is $2.1_{-0.9}^{+1.6} \times 10^{-14} \text{ erg s}^{-1} \text{ cm}^{-2}$ (90% posterior), and the photon index of the power-law is $\Gamma = 1.8 \pm 0.5$ (90% posterior). The fit is shown in Extended Data Fig. 4a.

1.1.3 *Swift*/XRT and the quiescent spectrum of AT2019qiz

We obtained Target of Opportunity Time to follow up AT2019qiz with the X-Ray Telescope (XRT) on-board the Neil Gehrels *Swift* Observatory (*Swift*). 11 observations were obtained from 2024-03-12 through 2024-03-14, with a typical exposure time of ≈ 1200 s per visit and cadence of 4.5 hours. We clearly detect one eruption in the new data (Fig. 1). We also re-analysed all previous XRT data for this source obtained under previous programs, using the online tools available through the UK *Swift* Science Data Centre [41, 42].

Due to the better sensitivity at soft energies compared to *Chandra*, we are able to model the underlying disk spectrum using the XRT observations during the quiescent phase. For this we use a color-corrected thermal disk model (TDEDISCSPEC) [43], to be consistent with the full spectral energy distribution fit (2.3). Given the larger PSF of XRT, we simultaneously model the AT2019qiz and the SE source contributions to the total spectrum. We use the model

$\text{TBABS} \times (\text{ZASHIFT}(\text{TDEDISCSPEC}) + \text{CFLUX}(\text{POW}))$, where $\text{ZASHIFT}(\text{TDEDISCSPEC})$ is the contribution from AT2019qiz and $\text{CFLUX}(\text{POW})$ is the contribution from the SE source. The fit does not require a redshifted absorption component. We employ `pyXSPEC` and `BXA`. For the disk parameters (i.e. AT2019qiz) we assume flat priors; however, for the SE source we use the posteriors from fitting its spatially resolved *Chandra* spectrum (1.1.2) as the priors. Extended Data Fig. 4b shows their individual contributions to the observed spectrum, confirming AT2019qiz dominates at energies below $\simeq 1.0$ keV. The posteriors of the fit indicate a peak disk temperature $kT_p = 67 \pm 10$ eV (90% posterior), in agreement with the bulk TDE population [44].

1.1.4 Archival data from *Swift*/XRT

The X-ray spectrum of AT2019qiz observed by *Swift*/XRT in 2019-2020 was reported to be hard [16, 21], suggesting a possible contribution from the SE source. To test this, we fit the combined spectrum (MJD 58714 to 59000) with the same power-law plus disk model. We again use our power-law fit posteriors for the SE source from *Chandra* as a prior in `BXA`, and this time fix the temperature of the disk component while letting its flux vary freely. The early-time XRT spectrum is entirely consistent with the SE source, with no statistically significant contribution from the disk component (Extended Data Fig. 4c). This results in a 3σ upper limit on the flux (0.3 – 1.0 keV) from AT2019qiz at early times of $\leq 1.4 \times 10^{-14}$ erg s $^{-1}$ cm $^{-2}$, or a luminosity $\leq 7.2 \times 10^{39}$ erg s $^{-1}$.

In contrast, AT2019qiz is brighter and detected at high significance in data from 2022 onwards, with a spectrum dominated by the thermal component [21]. AT2019qiz’s luminosity measured during all quiescent phases with XRT and *Chandra* is $\approx 10^{41}$ erg s $^{-1}$, more than an order of magnitude fainter than the eruptions. Extended Data Fig. 6 shows the observation from 2022 in bins of 5 ks. The final bin shows an increase in flux, but the temporal baseline is too short to confirm or rule out that this represents the onset of a QPE (see also Fig. 4). The spec-

tral fit from Ref. [21] is consistent with a blackbody with $kT_{BB} = 130 \pm 10$ eV, dominated by the final bin. We use the blackbody spectrum to calculate the luminosity in the final bin, and exclude this bin from the disk model fit in Fig. 4a. We stack the remaining counts in a single bin and compute the quiescent luminosity using the fit from Extended Data Fig. 4.

1.1.5 *NICER*

The Neutron Star Interior Composition Explorer (*NICER*) [45, 46] observed AT2019qiz in two distinct campaigns, first at early times (around optical peak) from 2019-09-25 to 2019-11-05 and another at late times (~ 1600 days after optical peak) from 2024-02-29 to 2024-03-09.

The cleaned events lists were extracted using the standard *NICER* Data Analysis Software (HEASoft 6.33.2) tasks `nicerl2` using the following filters: `nicersaafilt = YES`, `saafilt = NO`, `trackfilt = YES`, `ang_dist = 0.015`, `st_valid = YES`, `cor_range = "*-*`", `min_fpm = 38`, `underonly_range = 0-80`, `overonly_range = "0.0-1.0"`, `overonly_expr = "1.52 * COR SAX ** (-0.633)"`, `elv = 30` and `br_earth = 40`. The entire dataset was acquired during orbit night time and hence the daytime optical light leak (https://heasarc.gsfc.nasa.gov/docs/nicer/data_analysis/nicer_analysis_tips.html#lightleakincrease) does not apply to our data analysis. The latest *NICER* calibration release xti20240206 (06 February 2024) was used. Light curves in the 0.3–1.0 keV range were extracted using the `nicerl3-lc` task with a time bin size of 100 seconds and the SCORPEON background model.

The data obtained in the first campaign show no evidence for QPEs. Although the cadence is lower than that of the late-time data, it should be sufficient to detect QPEs occurring with the same frequency and duration as at late times, with a probability of detecting no QPEs of ≈ 0.02 (using binomial statistics with a 20% duty cycle). We can therefore likely rule out QPEs within the first ≈ 2 months after TDE fallback commenced (estimated to have occurred around 2019-09-11 [16]). However, we note that one would not expect QPEs during this phase in any model, as AT2019qiz was found to have an extended debris atmosphere [16], which remained

optically thick to X-rays until much later [21].

During the second observing campaign, we clearly detect QPEs. The field of view of *NICER* is shown in Extended Data Fig. 1, overlaid on the *Chandra* image. All of the sources detected by *Chandra* have intensities (at energies less than 1 keV) that is more than a factor of 10 below the measured peak of the QPE. Any contributions from these sources to the *NICER* spectra are further diminished by their offset angles from the centre of the field. We conclude that the *NICER* counts during eruptions are completely dominated by AT2019qiz. The six consecutive eruptions detected by *NICER* were modeled using a skewed Gaussian fit to each peak (Extended Data Fig. 2). We measure rest-frame delay times of 39.3 ± 0.3 , 56.3 ± 0.3 , 42.1 ± 0.3 , 51.2 ± 0.2 , and 53.5 ± 0.2 hours between successive eruptions.

Given the high count rate and good coverage we extracted time resolved X-ray spectra from the second *NICER* eruption (Fig. 1) in the 0.3-0.9 keV band. We created Good Time Intervals (GTIs) with the `nimaketime` for four intervals representing the Rise, Peak and Decay (two phases) of the eruption. We extracted these spectra using `nicerl3-spec` task, and produced SCORPEON background spectra in ‘file mode’ (`bkgmodeltype=scorpeon bkgformat=file`) for each of the four GTIs. We simultaneously fit the four spectra using `pyXSPEC` and `BXA`, assuming the model `TBABS×ZASHIFT(BBODY)`. We fixed the redshift to $z = 0.0151$ and included foreground absorption, with a fixed neutral hydrogen column density fixed to $n_H = 6.6 \times 10^{20} \text{ cm}^{-2}$ [47]. We initially included a redshifted absorber, but the model preferred zero contribution from this component, so we excluded it for simplicity. The full posteriors of the parameters are shown in Extended Data Fig. 3.

1.1.6 *AstroSat/SXT*

We observed AT2019qiz with *AstroSat* [48] for four days starting on 2024-03-12 UT using the Soft X-ray Telescope (SXT) [49] and the Ultra-Violet Imaging Telescope (UVIT) [50, 51]. We used the level2 SXT data processed at the Payload Operation Center using `sxtpipeline v1.5`.

We merged the orbit-wise level2 data using `SXTMerger.jl`. We extracted the source in 200 s bins using a circular region of 12 arcmin. The broad PSF of the SXT does not leave any source-free regions for simultaneous background measurement. However, the background is low (0.025 ± 0.002 counts s^{-1}) and steady. As the quiescent flux measured by *Chandra* is below the SXT detection limit, we take this count rate as our background estimate and subtract it from the light curve. SXT detected one eruption (MJD 60383.548).

1.2 Optical/UV Observations

1.2.1 *HST*

We observed AT2019qiz using *HST* on 2023-12-21 UT (MJD 60299.55), obtaining one orbit with the Wide-Field Camera 3 (WFC3) UVIS channel in the *F225W* band. We downloaded the reduced, drizzled and charge-transfer corrected image from the *HST* archive. We clearly detect a UV source coincident with the nucleus of the host galaxy. We verify this source is consistent with a point source both by comparing the profile to other point sources in the image using the `RADIALPROFILE` task in `PHOTUTILS`, and by confirming that the fraction of counts within apertures of 3 and 10 pixels are consistent with published encircled energy fractions in the UVIS documentation.

We perform aperture photometry using a 10 pixel (0.396 arcsecond) circular aperture, measuring the galaxy background per square arcsecond using a circular annulus between 20-40 pixels and subtracting this from the source photometry. Although we cannot measure the galaxy light at the precise position of AT2019qiz, having no UV images free from TDE light, the estimated background within our aperture is $< 2\%$ of the transient flux, so our results are not sensitive to this approximation. We correct to an infinite aperture using the encircled energy fraction of 85.8% recommended for *F225W*. The zeropoint is derived from the image header, including a chip-dependent flux correction. We measure a final magnitude of 20.63 ± 0.03 (AB).

While the angular scale of ~ 25 pc is not small enough to rule out a nuclear star cluster

(NSC), the UV source is an order of magnitude brighter than known NSCs [52]. Moreover, NSCs are generally red [53] and many magnitudes fainter than their host galaxies in bluer bands. The magnitude of the source we detect is comparable to the total UV magnitude of the galaxy [16]. An unresolved nuclear source was also detected in the QPE source GSN 069 [54].

1.2.2 Ground-based photometry

Numerous observations of this galaxy have been obtained by all-sky optical surveys both before and after the TDE. The optical emission was independently detected by ZTF [55, 56], the Asteroid Terrestrial Impact Last Alert System (ATLAS) [57], the Panoramic Survey Telescope and Rapid Response System (Pan-STARRS) [58] and the *Gaia* satellite [59].

Pan-STARRS reaches a typical limiting magnitude of ~ 22 in the broad w filter (effective wavelength of 6286 \AA) in each 45 s exposure. All observations are processed and photometrically calibrated with the PS image processing pipeline [60, 61, 62]. We downloaded and manually vetted all w -band observations of AT2019qiz since September 2019, and in most cases confirm a clean subtraction of the host galaxy light. We also retrieved ZTF forced photometry [63] in the r -band (with a similar effective wavelength of 6417 \AA). Due to the shallower limiting magnitude of ~ 20.5 , we stack the fluxes in 7 day bins. Both surveys clearly detect an ongoing plateau, persisting for > 1000 days with a luminosity $\nu L_\nu \sim 7 \times 10^{40} \text{ erg s}^{-1}$. All Pan-STARRS and ZTF photometry was measured after subtraction of pre-TDE reference images using dedicated pipelines, and hence include only light from AT2019qiz.

While the optical light curves show scatter consistent with noise, they do not appear to exhibit the intense flaring behaviour seen in the X-rays. An order-of-magnitude flare in the optical would easily be detected even in the unbinned ZTF photometry. Assuming a duty cycle of 20%, and conservatively restricting to data since January 2022 (when we first see signs of day-timescale X-ray variability with XRT), the probability of never detecting an eruption simply due to gaps in cadence is $\lesssim 10^{-13}$.

To test for optical variability on shorter timescales, we conducted targeted observations with the 1.8 m Pan-STARRS2 telescope in Hawaii on 2024-02-11, with the IO:O instrument on the 2.0 m Liverpool Telescope [64] (LT) in La Palma on 2024-02-15, and with ULTRACAM [65] on the 3.5 m New Technology Telescope at the European Southern Observatory (La Silla) in Chile on 2024-02-10. Pan-STARRS images were obtained in the w band (50×200 s exposures) and LT in the r band (32×120 s), while ULTRACAM observed simultaneously in u_s, g_s, r_s bands [66] (384×20 s, with only 24 ms between exposures). All images were reduced through standard facility pipelines. For Pan-STARRS, this included subtraction of a pre-TDE reference image and forced photometry at the position of AT2019qiz. In the case of LT and ULTRACAM, we performed photometry using PSF [67], an open-source PYTHON wrapper for PHOTUTILS and other image analysis routines. We excluded 17 ULTRACAM images affected by poor seeing. We attempted manual subtraction of the Pan-STARRS reference images using PSF, however we found that the additional noise introduced by the subtraction was larger than any detectable variability. As shown in Extended Data Fig. 5, there is no strong evidence for variability on timescales \sim hours.

1.2.3 *Swift*/UVOT

UV observations were taken with *Swift*/UVOT in the *uvm2* filter contemporaneously with the XRT observations. We used the `uvotsource` package to measure the UV photometry, using an aperture of $12''$. We subtracted the host galaxy contribution by fitting archival photometry data with stellar population synthesis models using PROSPECTOR [68]. This standard procedure has been used to analyse previous UVOT observations of TDEs [56]. We apply Galactic extinction correction to all bands using $E(B - V)$ value of 0.094 [69].

The UVOT photometry is shown in Extended Data Fig. 5. Although lacking the resolution of *HST* to separate the central point source from the host light, the mean measured magnitude of 20.1 is ~ 0.5 mag brighter than the host level estimated by SED modeling [16]. The individual

measurements exhibit root-mean-square variation of 0.27 mag (Extended Data Fig. 5), possibly indicating variability that would further exclude a nuclear star cluster. The timing of the XRT QPE is marked, coinciding with a possible (but not statistically significant) dip in UV flux as seen in the QPE candidate XMMLS1 J0249 [13].

1.2.4 *AstroSat/UVIT*

We observed AT2019qiz with the UV Imaging Telescope (UVIT) using the broad filter CaF2 (F148W) [50]. We processed the level1 data with the CCDLAB pipeline [70], and generated orbit-wise images, detecting a bright nuclear source. We performed aperture photometry using UVITTools.jl package and the latest calibration [51], in a circular region of 20 pixels (8.2 arcsec). We also extracted background counts from a source-free area of the image. The background-corrected count rate in the merged image corresponds to a flux density $f_\lambda = 3.16 \pm 0.97 \times 10^{-16} \text{ erg cm}^{-2} \text{ s}^{-1} \text{ \AA}^{-1}$ or magnitude $m = 20.49 \pm 0.03$ (AB). We found no statistically significant FUV variability between the orbit-wise images. We do not attempt to remove host galaxy flux for the UVIT data, as the field has not been covered by previous FUV surveys. SED modelling would require a large extrapolation. Regardless, we expect that the galaxy flux should be negligible at these wavelengths [20].

2 Analysis

2.1 Assessing variability

We perform two checks that the X-ray variability corresponds to QPEs rather than random variation. First we compare to physically-motivated models of stochastic variability. Ref. [71] demonstrated a mechanism to produce order-of-magnitude X-ray variability through Wien-tail amplification of accretion disk perturbations. Their Figure 3 shows the X-ray light curve of a model with a SMBH mass of $2 \times 10^6 M_\odot$, consistent with AT2019qiz. The light curves are of a visibly different character to our data, with random variability rather than flares of consistent

duration, and no obvious ‘quiescent’ level. We ran additional simulations using their model, and never found a light curve segment resembling AT2019qiz.

We also take a model-agnostic approach and assume the null hypothesis that the times of the X-ray peaks are random. Drawing a list of 10^5 delay times from a flat probability distribution between 0 – 60 hours, and examining every consecutive sequence of eight, we ‘measure’ the standard deviation in delay times to be $\leq 15\%$ of the mean in only $\lesssim 0.1\%$ of trials. This is not sensitive to where we place the upper and lower bounds of the distribution. Therefore we can exclude random peak times at $> 3\sigma$ confidence.

2.2 QPE duration-recurrence time correlation

The data in Fig. 3a show an apparent correlation between the mean duration and mean recurrence time of QPEs from a given source [5]. An equivalent statement is that QPEs appear to show a constant duty cycle across the population, with previous work indicating a duty cycle 0.24 ± 0.13 [5]. We reanalyse this correlation including AT2019qiz by performing Bayesian regression with a linear model $T_{\text{duration}} = \alpha T_{\text{recurrence}} + \beta$. We find $\alpha = 0.22^{+0.11}_{-0.04}$ (95% credible range), consistent with previous findings [5]. Comparing this model to the null hypothesis ($\alpha = 0$) we find a change in the Bayesian Information Criterion $\Delta\text{BIC} \approx 50$, indicating a strong preference for a positive linear correlation over the null hypothesis of no correlation.

2.3 Disk modeling

We use the time dependent relativistic thin disk model developed in Refs. [25, 19]. This computes the spectrum of an evolving accretion flow, produced at early times by the circularisation of some fraction of the TDE stellar debris. To generate light curves we follow the procedure of Ref. [19] (their Figure 2). The important input parameters are the mass and spin of the SMBH, the initial disk mass, the disk-observer inclination angle, and the turbulent evolutionary timescale. In addition, there are nuisance parameters relating to the initial surface density pro-

file of the disk, which is generally unknown and has minimal effect on the late-time behaviour. As this initial condition is so poorly constrained, we simply consider an initial ring of material (as in Ref. [25]).

For each set of parameters $\{\Theta\}$, we compute the total (log-)likelihood

$$\mathcal{L}(\Theta) = - \sum_{\text{bands}, i} \sum_{\text{data}, j} \frac{(O_{i,j} - M_{i,j})^2}{E_{i,j}^2}, \quad (1)$$

where $O_{i,j}$, $M_{i,j}$ and $E_{i,j}$ are the observed flux, model flux and flux uncertainty of the j^{th} data point in the i^{th} band respectively. For the X-ray data we compute the integrated 0.3 – 1 keV flux using the best-fit models to the quiescent *Swift*/XRT and *Chandra* data, while for optical/UV bands we compute the flux at the effective frequency of the band. We correct all data for foreground extinction/absorption [69, 47].

The early optical and UV observations do not probe direct emission from the accretion flow, either due to reprocessing [72] or shock emission from streams [73]. We add an early time component to model out this decay [19], with functional form

$$L_{\text{early}} = L_0 \exp(-t/\tau_{\text{dec}}) \times \frac{B(\nu, T)}{B(\nu_0, T)}, \quad (2)$$

where $B(\nu, T)$ is the Planck function, and $\nu_0 = 6 \times 10^{14}$ Hz is a reference frequency. We fit the amplitude L_0 , temperature T and decay timescale τ_{dec} in addition to the disk parameters. We only include data taken after the peak of the optical light curves.

The fit was performed using Markov Chain Monte Carlo techniques, employing the EMCEE formalism [74]. To speed up computations, analytic solutions of the relativistic disk equations [75] were used. The model satisfactorily reproduces all data. The model X-ray light curve shows a slow rise, however this is completely unconstrained by data and is therefore very sensitive to the uncertain initial conditions of the simulation. After a few hundred days (by the time of the earliest X-ray data in Fig. 4), the disk has spread to large radii and is no longer sensitive to initial conditions. We present the posterior distributions of the physically relevant free

parameters in Extended Data Fig. 8. The best-fitting SMBH mass is consistent with all other observational constraints.

We note that a dimensionless SMBH spin parameter $a_{\bullet} > 0$ is favoured by the model (though see caveats below), with a peak in the posterior around $a_{\bullet} \sim 0.4 - 0.5$. This constraint originates from the relative amplitudes of the optical/UV and X-ray luminosities, as is highlighted in Extended Data Fig. 9. As the optical and UV light curves are well separated in frequency, the properties of the disk at scales $r \gtrsim 20r_g$ are tightly constrained. The amplitude of the X-ray luminosity is controlled by the temperature of the inner disk, close to the innermost stable circular orbit (ISCO). For a given large-scale structure, this radius is determined by a_{\bullet} .

Our disk model parameterizes the color correction factor f_{col} in terms of the local disk temperature [76], but our posteriors do not marginalize over its unknown uncertainty. Recognizing that modest uncertainties in f_{col} lead to substantial uncertainties in spin (for non-maximal black hole spins) [77], we do not claim a spin measurement here, but simply note that a modest spin is consistent with our data. The spin estimates in this model also assume a planar disk that is aligned with the SMBH spin, which is not true in the case of a precessing disk (see next section).

While the disk temperature profile (and therefore the location of the disk’s outer edge) is tightly constrained from the multi-band late-time observations, it is well known that disk temperature constraints only probe the product $W_{\phi}^r \Sigma$, where W_{ϕ}^r is the turbulent stress and Σ is the surface mass density. As the functional form of the turbulent stress cannot be derived from first principles, and must be specified by hand, there is some uncertainty in the mid-disk density slope. Our choice of W_{ϕ}^r parameterisation is optimized for computational speed [75], and is given by $W_{\phi}^r = w = \text{constant}$. Rather than fit for w , we fit for the evolutionary timescale of the disc (which has a more obvious physical interpretation), given by $t_{\text{evol}} \equiv 2\sqrt{GM_{\bullet}r_0^3}/9w$. We emphasise that this uncertainty has no effect on our constraints on the size of the disk.

With this choice of parameterization for the turbulent stress, the disk density profile (Fig. 4) can be approximated as $\Sigma \propto r^{-\zeta}$, with $\zeta = 1/2$, for $r = (2 - 600)GM_{\bullet}/c^2$. The density slope

is not very sensitive to modelling assumptions, with the (potentially) more physical radiation pressure dominated α -disk model having $\zeta = 3/4$.

2.4 Precession timescales

If the SMBH is rotating, any orbit or disk that is misaligned with the spin axis will undergo Lense-Thirring precession. This is a possible cause of timing variations in QPEs [30]. Changes in QPE timing in AT2019qiz are seen over the course of $\lesssim 8$ observed cycles, which would require that the precession timescale is $T_{\text{prec}} \sim \text{few} \times T_{\text{QPE}}$, where $T_{\text{QPE}} \approx 48.4$ hr is the QPE recurrence time.

The precession timescale can be calculated following [29]:

$$T_{\text{prec}} = \frac{8\pi GM_{\bullet}(1 + 2\zeta)}{c^3(5 - 2\zeta)} \frac{r_{\text{out}}^{5/2-\zeta} r_{\text{in}}^{1/2+\zeta} (1 - (r_{\text{in}}/r_{\text{out}})^{5/2-\zeta})}{a_{\bullet}(1 - (r_{\text{in}}/r_{\text{out}})^{1/2+\zeta})}, \quad (3)$$

where r_{in} and r_{out} are the inner and outer radii of the disk or orbit, in Schwarzschild units (see also [78]). We assume $\log(M_{\bullet}/M_{\odot}) = 6.3$, and investigate the plausible precession period for different values of a_{\bullet} .

The nodal precession timescale for an orbiting body can be estimated by calculating T_{prec} at the orbital radius (setting $R_{\text{in}} \approx R_{\text{out}} \approx R_{\text{orb}}$). For $a_{\bullet} = 0.1 - 0.9$, this gives $T_{\text{prec,orbit}} \approx (10^3 - 10^4) \times T_{\text{QPE}}$, independent of ζ . Therefore in the EMRI model, nodal precession is too slow to account for changes in QPE timing over a few orbits.

The precession timescale of the disk can be calculated by assuming it behaves as a rigid body with $r_{\text{in}} = 2GM_{\bullet}/c^2$, $r_{\text{out}} = 600GM_{\bullet}/c^2$ and a density slope $\zeta = 1/2$ from our disk model. We use the equation above to find $T_{\text{prec,disk}} \approx (70 - 200) \times T_{\text{QPE}}$ (for the same range of spins). With a steeper density profile having $\zeta = 1$, this would reduce to $T_{\text{prec,disk}} \approx (8 - 70) \times T_{\text{QPE}}$ (since more mass closer to the SMBH enables stronger precession). Therefore precession can explain detectable changes in QPE timing over the course of a few orbits only in the case of a rapidly spinning SMBH ($a_{\bullet} \gtrsim 0.5 - 0.7$) and a steep disk density profile.

With these constraints, attributing the timing residuals primarily to disk precession becomes challenging. The larger the SMBH spin magnitude, the faster an initially inclined disk will come into alignment with the BH spin axis, damping precession on a timescale $\lesssim 100$ days for $a_{\bullet} > 0.6$ and $M_{\bullet} \sim 10^6 M_{\odot}$ [79]. To maintain precession for over 1000 days requires a spin $a_{\bullet} \lesssim 0.2$, in which case the precession is not fast enough to fully explain the timing variations in our data.

We also note that the disk inner radius used in our precession calculation was derived from a planar disk model. In a tilted disk around a spinning SMBH, the radius of the ISCO will differ from the equatorial case. Understanding the effect of disk precession in AT2019qiz will likely require both continued monitoring to better understand the QPE timing structure, and a self-consistent model of an evolving and precessing disk that can explain both the multi-wavelength light curve and timing residuals.

2.5 Constraints on QPE models

Many models have been proposed to explain QPEs. Disk tearing due to Lense-Thirring precession has been suggested [80]. This effect has plausibly been detected in the TDE AT2020ocn [81], however its X-ray light curve did not resemble that of AT2019qiz or those of other QPEs. As discussed above, it is also unclear whether strong precession will persist until such late times. The X-ray variability in AT2020ocn occurred only in the first months following the TDE.

Gravitational lensing of an accretion disk by a second SMBH in a tight binary could cause periodic X-ray peaks for the right inclination [82]. However, in the case of AT2019qiz no signs of gravitational self-lensing were detected during the initial TDE. In this model a QPE magnification by a factor $\gtrsim 10$ requires an extremely edge-on view of the disk, which leads to a shorter duration of the QPE flares. This was already problematic for previous QPEs [82], and is more so for the longer-duration flares in AT2019qiz. Moreover, finding a TDE around a close SMBH binary within a very narrow range of viewing angles ($\gtrsim 89.5^{\circ}$) is very unlikely

within the small sample of known TDEs, so a strong TDE-QPE connection is not expected in this model.

Limit cycle instabilities are an appealing way to explain recurrent variability [7], [83]. The recurrence timescale for disk pressure instabilities depends on whether the disk is dominated by radiation pressure or magnetic fields [8], as well as the accretion rate. Our disk model, which is well constrained by the multi-wavelength data, gives an Eddington ratio $\dot{M}/M_{\text{Edd}} \approx L/L_{\text{Edd}} = 0.04 \pm 0.01$. Ref. [26] give formulae to interpolate the recurrence time for radiation pressure instabilities, for a given amplitude relative to quiescence. We assume a peak-to-quiescence luminosity ratio of 60, though our analysis is not sensitive to this. Using either the prescription for intermediate-mass BHs (their equation 33) or SMBHs (their equation 34), we find a recurrence time of ~ 5000 days.

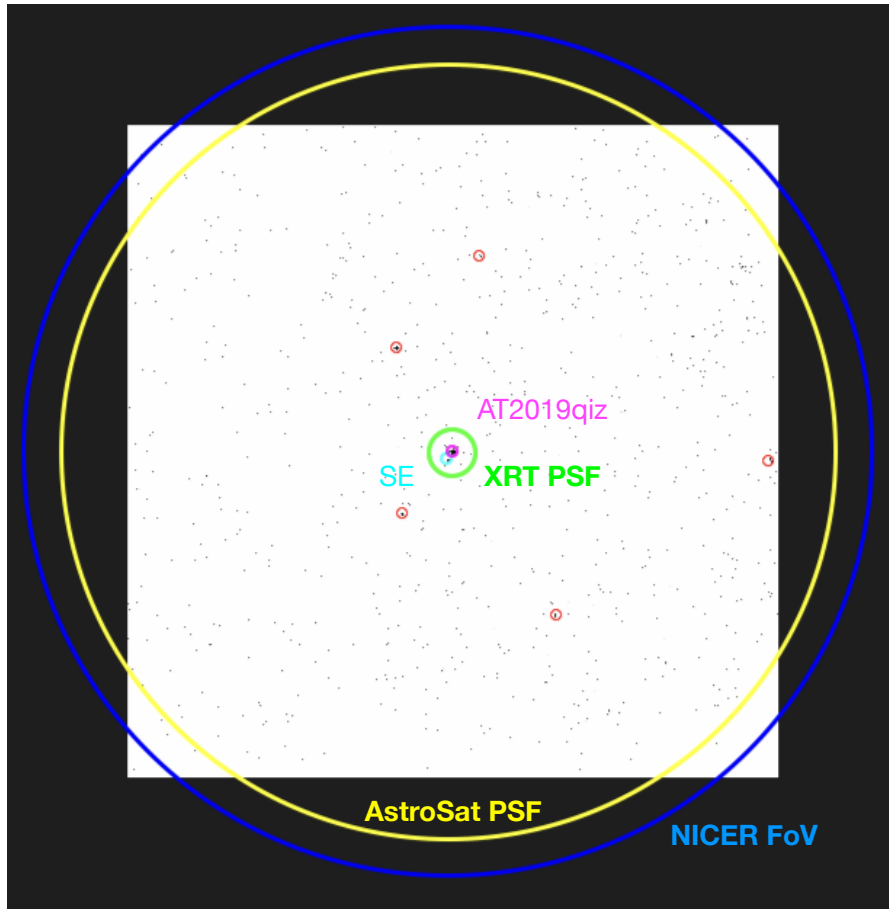
In the magnetic case, we use equation 14 from Ref. [8]. Matching the observed recurrence time requires a dimensionless magnetic pressure scaling parameter $p_0 \sim 10$. However, at this Eddington ratio the disk should be stable [8] if $p_0 \gtrsim 1$. This leaves no self-consistent solution in which magnetic pressure instabilities cause the QPEs in AT2019qiz. The possibility of a long-short cycle in recurrence time, and the asymmetric profile of the eruptions [3], also disfavour pressure instabilities. We also note that in disk instability models, the recurrence time of the instability correlates with SMBH mass. For the known QPEs, there is no apparent correlation in recurrence time with mass (Fig. 3).

The final class of models to explain QPEs involves an orbiting body (EMRI) either transferring mass to an accretion disk or colliding with it repeatedly [9, 10, 28, 11, 35, 30, 27], [84, 85, 86]. Note that this is very unlikely to be the same star that was disrupted during the TDE: if a bound remnant survived the disruption, it is expected to be on a highly eccentric orbit with a much longer period than the QPEs [11]. The fundamental requirement for star-disk collisions to explain QPEs is that the disk is wider than the orbit of the EMRI. The size of the disk in AT2019qiz is well constrained by our analysis, and the posteriors of our fit fully satisfy this

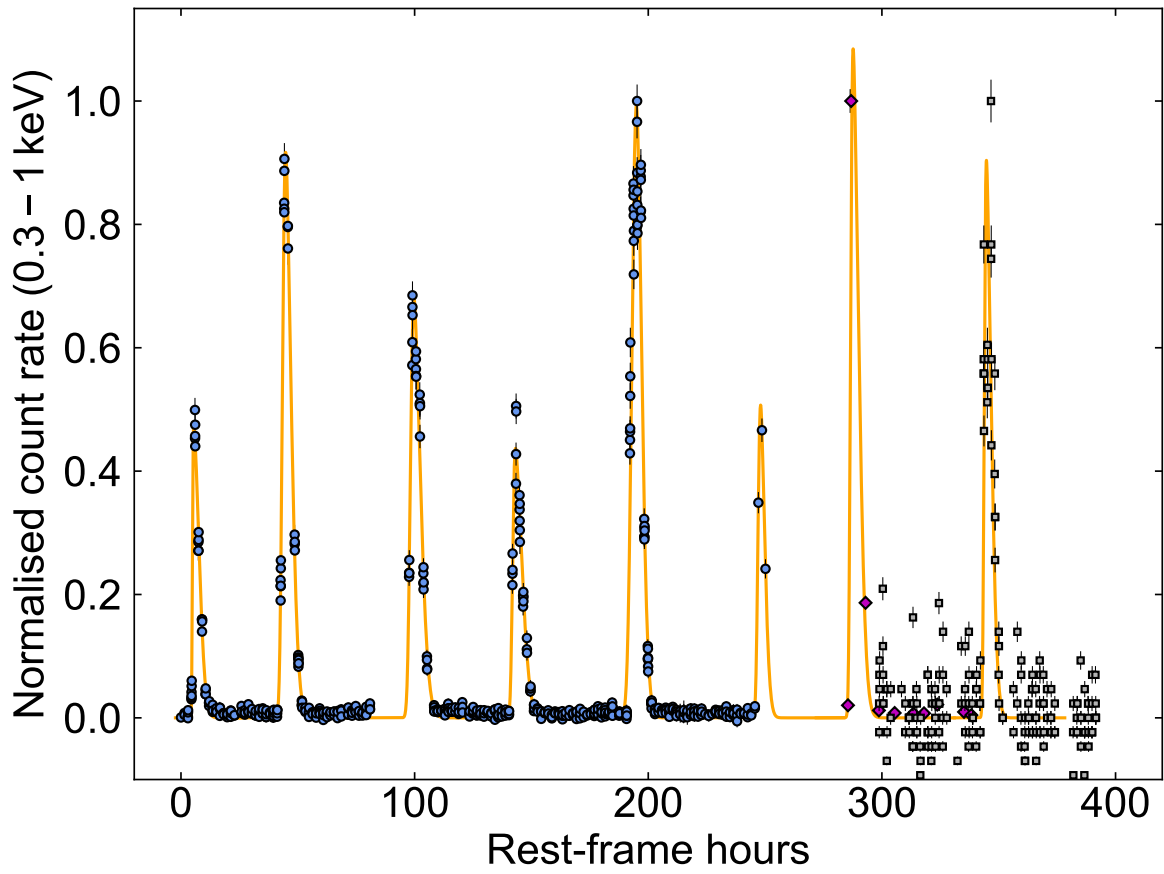
requirement, at least in the case of a circular disk.

For an orbit with the QPE period to avoid intersecting the disk would require a disk ellipticity $e > 0.7$ (assuming the semi-major axis of the disk is fixed) and an appropriately chosen orbital inclination. While some TDE spectra support a highly elliptical disk in the tens of days after disruption [87], most can be explained with an approximately circular disk [88, 89, 90]. Simulations of TDE accretion disks show a high ellipticity in the days after disruption [91], but shocks are expected to circularise the disk over the course of a few debris orbital periods [92] (days to weeks) whereas we observe QPEs on timescales of years after AT2019qiz. An initially highly eccentric disk becomes only mildly elliptical ($e \sim 0.6$) on timescales of a few days [93]. Once significant fallback has ceased (before the plateau phase), no more eccentricity will be excited in the disk, while turbulence will act to further circularise it, so we expect the disk in AT2019qiz will be circular to a good approximation.

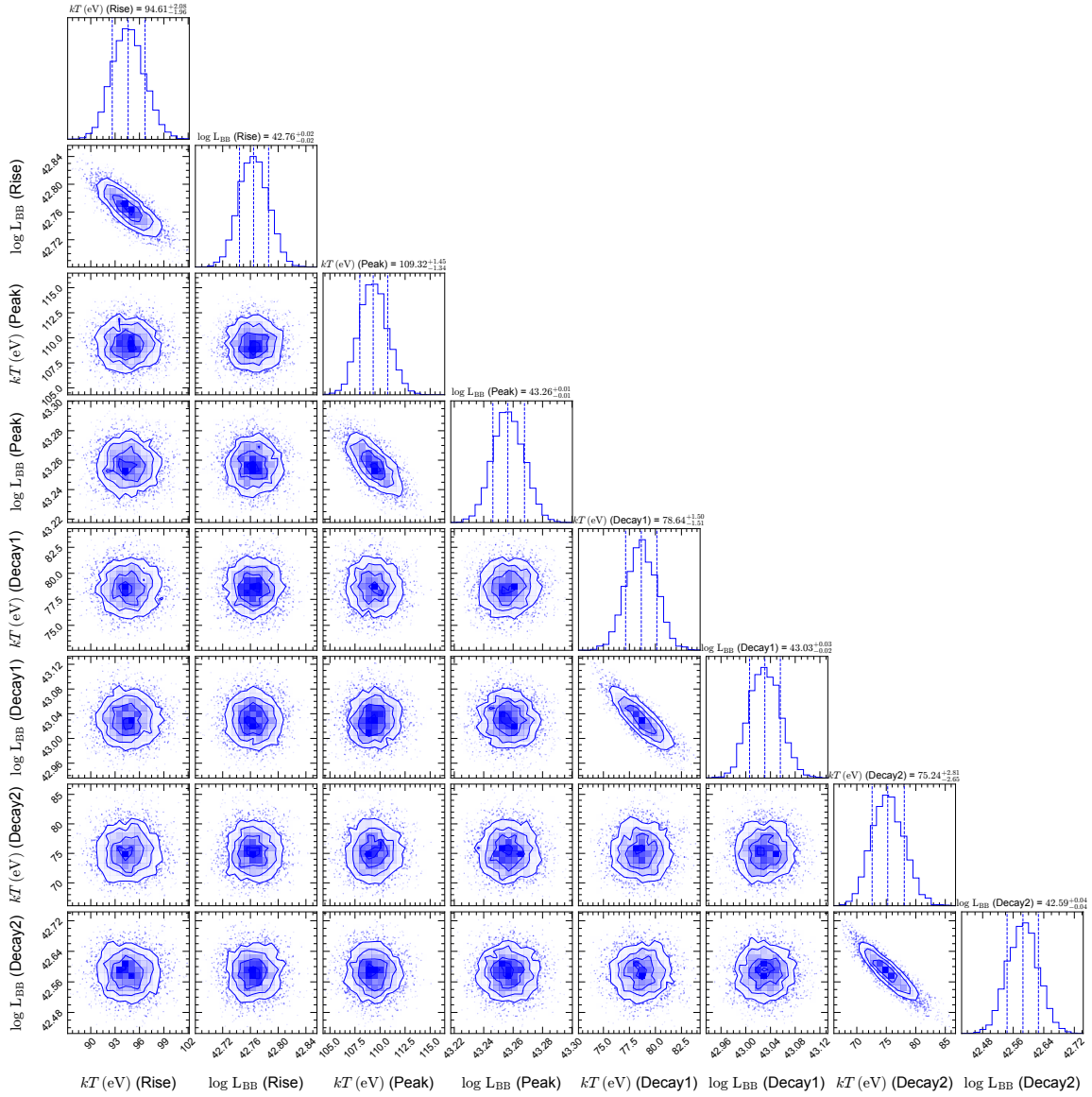
The case of an EMRI interacting with a TDE disk was specifically predicted by Refs. [11, 30]. The formation rate of EMRIs by the Hills mechanism is $\sim 10^{-5} \text{ yr}^{-1} \text{ galaxy}^{-1}$, about one tenth of the TDE rate. Since the time for inspiral via gravitational wave emission ($\sim 10^6 \text{ yr}$) is longer than the time between TDEs ($\sim 10^4 \text{ yr}$), theory predicts that $\gtrsim 1$ in 10 TDEs could host an EMRI capable of producing QPEs [11, 35]. This is consistent with recent observational constraints on the QPE rate [24].



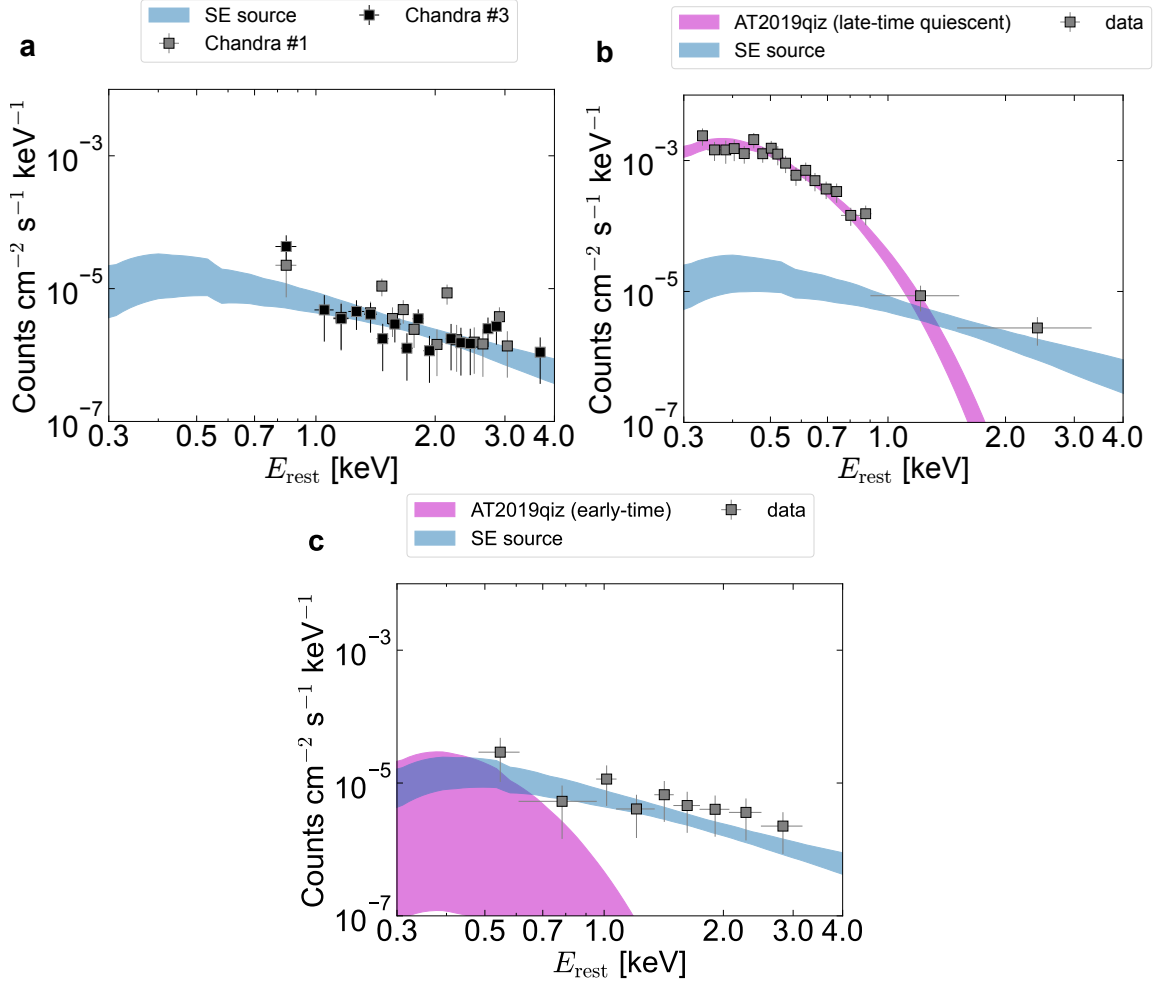
Extended Data Figure 1: ***Chandra* image during eruption.** The image is 8.5×8.5 arcmin, with North up and East to the left. Five sources are detected within a few arcminutes of AT2019qiz. Only AT2019qiz shows statistical evidence of variability in the *Chandra* data (Methods). The point-spread functions (half-encircled energy width) of *Swift*/XRT and AstroSat are marked, as is the *NICER* field-of-view. None of the sources exhibit a count rate (0.3 – 1 keV) above $\sim 10\%$ of the count rate from AT2019qiz during eruption. Fig. 1a shows a zoom-in of the central region.



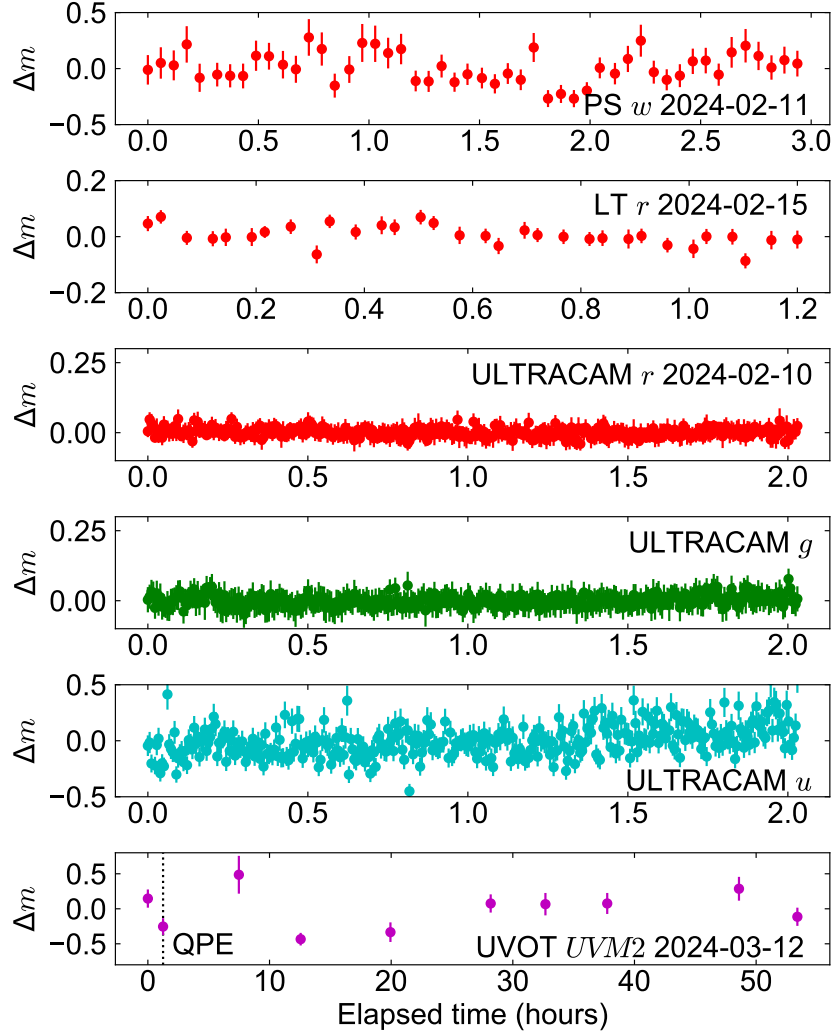
Extended Data Figure 2: **Estimates of the peak times of each eruption.** Each peak has been fit separately with a skewed Gaussian function using SCIPY. This takes four parameters: the mean μ of the unskewed Gaussian, the standard deviation σ , the skewness a , and an arbitrary normalisation. We take the maximum of the function as the time of each peak. The uncertainty in timing is given by the variance in μ . The error bars show the 1σ uncertainty in count rate.



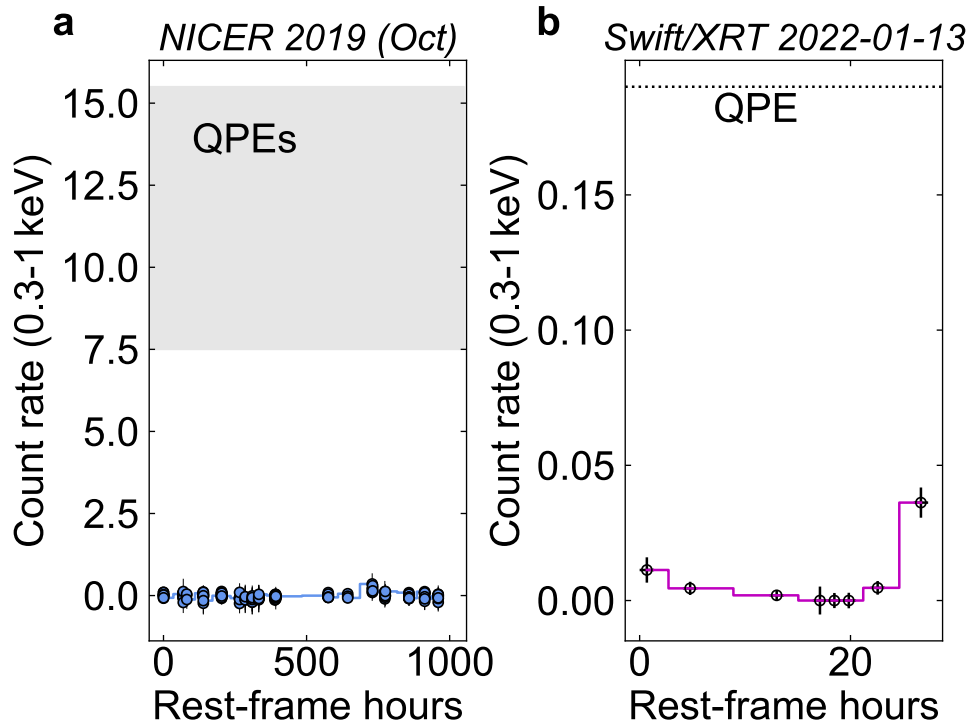
Extended Data Figure 3: **Physical parameters from the second eruption detected with *NICER*.** Corner plot showing posterior distributions of all free parameters from the time-resolved spectral modelling of the second *NICER* eruption (Fig. 2).



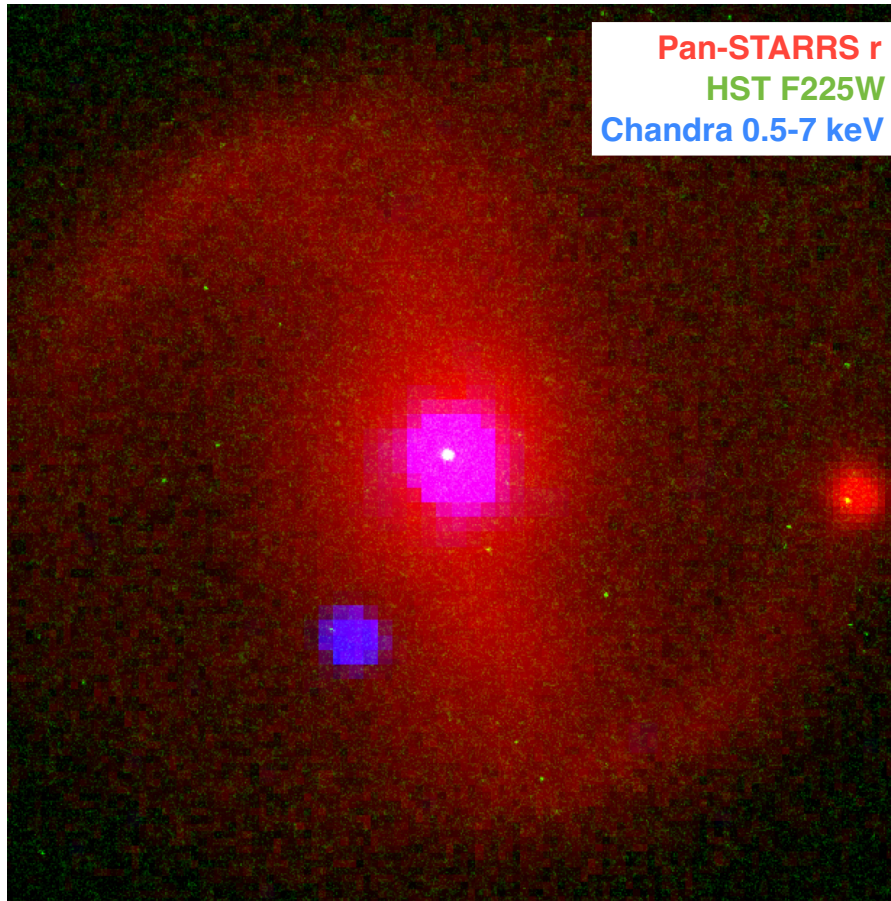
Extended Data Figure 4: **Fits to the quiescent spectrum of AT2019qiz and the nearby SE source.** Shaded regions show 90% confidence intervals. **(a)** Fit to the SE source from *Chandra* (first and third epochs). The data are best fit with a power-law with $\Gamma = 1.8 \pm 0.5$. **(b)** Fit to the quiescent spectrum from *Swift*/XRT. This includes flux from both sources. We fit with a power-law plus a thermal disk model including colour correction (TDEDISCSPEC), using the posteriors from the SE source as the priors on the power-law component. The SE source clearly dominates the count rate above $\simeq 1$ keV. Below this, the spectrum is well fit by the thermal disk with peak temperature of $kT_p = 67 \pm 10$ eV, similar to other QPE sources during their quiescent phases [1, 3], and similar to X-ray detected TDEs [44]. The SE source contribution is shown in blue. **(c)** Fit to the X-ray spectrum during the initial phase of the TDE optical component (MJD 58714 to 59000) using the temperature and power-law slope from panels (a) and (b). The spectrum is consistent with emission from the SE source, with no statistically significant contribution from AT2019qiz.



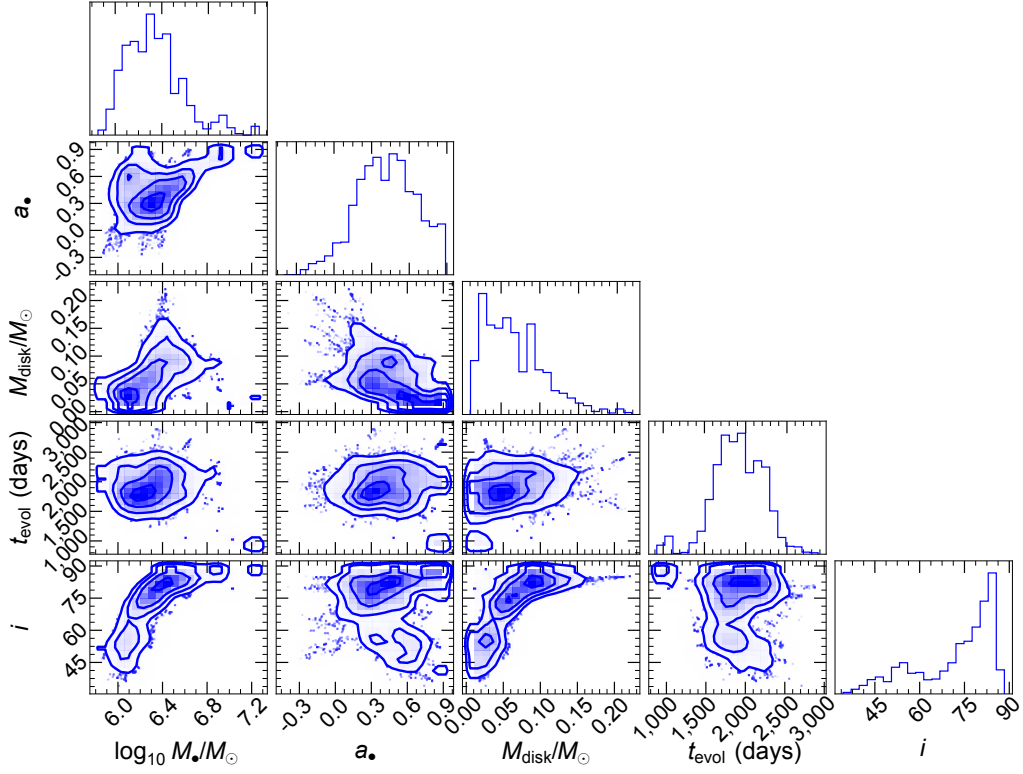
Extended Data Figure 5: **High-cadence optical observations and UV photometry.** Pan-STARRS data are measured on difference images using the Pan-STARRS reference image for subtraction, whereas for LT, ULTRACAM and UVOT we measure aperture photometry on the unsubtracted images. We subtract the mean magnitude in each case to emphasise the (lack of) strong variability on hour-long timescales. However, the UV shows possible variability at the level of a few $\times 0.1$ mag, with a possible dip at the time of the QPE [13]. Note that the time axis is different on each sub-plot, and the dates on which each data set was obtained are provided on the individual panels. The error bars show the 1σ uncertainty in magnitude.



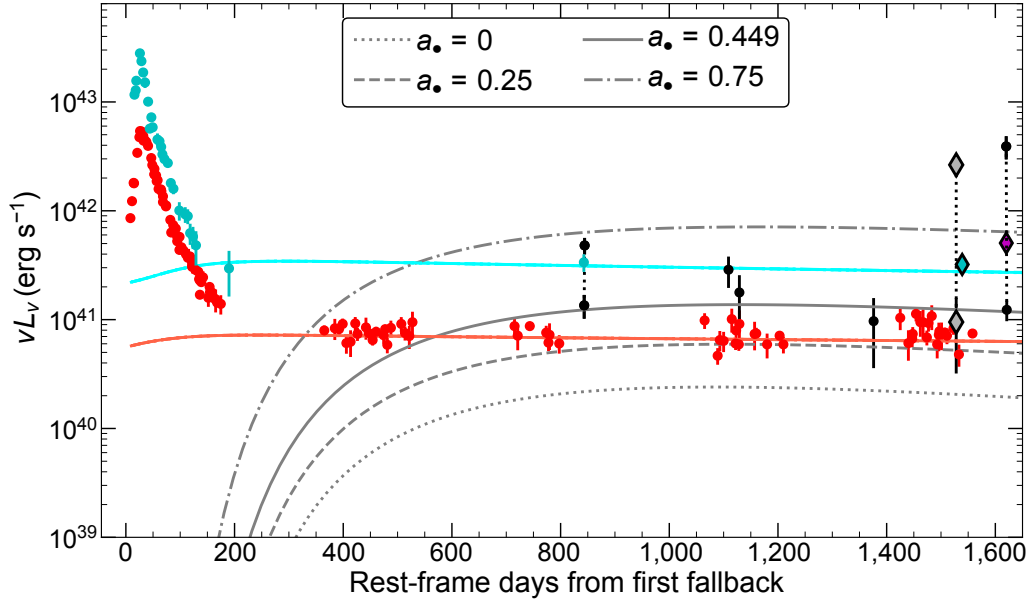
Extended Data Figure 6: **High-cadence X-ray observations at earlier times.** (a) *NICER* data obtained between 2019-09-25 and 2019-11-05, close to the time of the optical TDE peak. No variability is detected, with the shaded region showing the range of QPE peaks at late times. Comparing to the observed QPEs at late times suggests we would have most likely detected ≈ 2 QPEs if they were active. (b) *Swift* XRT data [21] obtained on 2022-01-13, binned in 5 ks fixed bins. The dashed line shows the QPE later detected with XRT. Variability is now observed on \sim hour timescales, but the baseline is insufficient to determine if this is QPE-like in nature. The error bars show the 1σ uncertainty in count rate.



Extended Data Figure 7: **Optical, UV and X-ray images.** 30 by 30 arcsecond false-colour image, centered at the position of AT2019qiz. The red channel shows the archival Pan-STARRS stacked image of the field in r -band. The blue channel shows the *Chandra* image during the QPE (which appears magneta overlaid on the red Pan-STARRS image), smoothed with a 2 pixel Gaussian filter. The green channel shows the *HST* image, demonstrating the point nature of the UV emission (visible as a white dot at the centre of the image), and its association with the host nucleus.



Extended Data Figure 8: **Parameter constraints from the disk model.** The posterior distributions of the model fit to AT2019qiz. The SMBH mass posterior (M_{\odot}) is consistent with all other observational constraints, and all other parameter values are in the expected range for TDEs. The SMBH spin is denoted a_{\bullet} , M_{disk} is the initial disk mass, t_{evol} parameterises the timescale of viscous spreading, and i is the inclination of the disk with respect to the observer.



Extended Data Figure 9: **Examples of disk model light curves for four different SMBH spin values.** All other parameters are fixed to the posterior medians. The colours are the same as Fig. 4. In optical and UV bands, varying the spin produces imperceptible changes in the light curves, but in the X-ray band the changes are pronounced. Physically, this is due to the exponential sensitivity of the X-ray flux on the inner disc temperature, whereas the optical and UV luminosity is sensitive only to the disk structure at larger radii.

Method	$\log(M_{\bullet}/M_{\odot})$	Uncertainty	Source
Galaxy scaling relations			
$M_{\bullet} - \sigma$ [94]	6.54	0.32	[16]
$M_{\bullet} - \sigma$ [95]	6.24	0.48	[16]
$M_{\bullet} - \sigma$ [96]	5.82	0.41	[16]
Light curve modeling			
MOSFIT [97, 98]	5.89	0.21	[16]
MOSFIT [97, 98]	6.14	0.1	[17]
MOSFIT [97, 98]	6.22	0.2	[99]
TDEMASS [100]	6.18	0.07	[100]
TDE scaling relations			
L_{plateau} [19]	5.42	+0.58, -0.45	[19]
L_{peak} [19]	6.13	0.5 (sys. only)	[19]
E_{rad} [19]	6.35	0.5 (sys. only)	[19]
Disk modeling [25]	6.3	+0.3, -0.2	This work

Extended Data Table 1: **Estimates of the SMBH mass in AT2019qiz.** Errors represent the 1σ uncertainty including statistical and systematic errors unless otherwise specified.

References

- [1] Miniutti, G. *et al.* Nine-hour X-ray quasi-periodic eruptions from a low-mass black hole galactic nucleus. *Nature* **573**, 381–384 (2019).
- [2] Giustini, M., Miniutti, G. & Saxton, R. D. X-ray quasi-periodic eruptions from the galactic nucleus of RX J1301.9+2747. *Astron. Astrophys.* **636**, L2 (2020).
- [3] Arcodia, R. *et al.* X-ray quasi-periodic eruptions from two previously quiescent galaxies. *Nature* **592**, 704–707 (2021).
- [4] Arcodia, R. *et al.* The more the merrier: SRG/eROSITA discovers two further galaxies showing X-ray quasi-periodic eruptions. *Astron. Astrophys.* **684**, A64 (2024).
- [5] Guolo, M. *et al.* X-ray eruptions every 22 days from the nucleus of a nearby galaxy. *Nat. Astron.* (2024).
- [6] Pan, X., Li, S.-L., Cao, X., Miniutti, G. & Gu, M. A Disk Instability Model for the Quasi-periodic Eruptions of GSN 069. *Astrophys. J. Lett.* **928**, L18 (2022).
- [7] Śniegowska, M., Grzędzielski, M., Czerny, B. & Janiuk, A. Modified models of radiation pressure instability applied to 10 , 10^5 , and $10^7 M_{\odot}$ accreting black holes. *Astron. Astrophys.* **672**, A19 (2023).
- [8] Kaur, K., Stone, N. C. & Gilbaum, S. Magnetically dominated discs in tidal disruption events and quasi-periodic eruptions. *Mon. Not. R. Astron. Soc.* **524**, 1269–1290 (2023).
- [9] Dai, L. J., Fuerst, S. V. & Blandford, R. Quasi-periodic flares from star-accretion-disc collisions. *Mon. Not. R. Astron. Soc.* **402**, 1614–1624 (2010).

- [10] Xian, J., Zhang, F., Dou, L., He, J. & Shu, X. X-Ray Quasi-periodic Eruptions Driven by Star-Disk Collisions: Application to GSN069 and Probing the Spin of Massive Black Holes. *Astrophys. J. Lett.* **921**, L32 (2021).
- [11] Linial, I. & Metzger, B. D. EMRI + TDE = QPE: Periodic X-Ray Flares from Star-Disk Collisions in Galactic Nuclei. *Astrophys. J.* **957**, 34 (2023).
- [12] Miniutti, G. *et al.* Repeating tidal disruptions in GSN 069: Long-term evolution and constraints on quasi-periodic eruptions' models. *Astron. Astrophys.* **670**, A93 (2023).
- [13] Chakraborty, J. *et al.* Possible X-Ray Quasi-periodic Eruptions in a Tidal Disruption Event Candidate. *Astrophys. J. Lett.* **921**, L40 (2021).
- [14] Quintin, E. *et al.* Tormund's return: Hints of quasi-periodic eruption features from a recent optical tidal disruption event. *Astron. Astrophys.* **675**, A152 (2023).
- [15] Wevers, T., Pasham, D. R., Jalan, P., Rakshit, S. & Arcodia, R. Host galaxy properties of quasi-periodically erupting X-ray sources. *Astron. Astrophys.* **659**, L2 (2022).
- [16] Nicholl, M. *et al.* An outflow powers the optical rise of the nearby, fast-evolving tidal disruption event AT2019qiz. *Mon. Not. R. Astron. Soc.* **499**, 482–504 (2020).
- [17] Hung, T. *et al.* Discovery of a Fast Iron Low-ionization Outflow in the Early Evolution of the Nearby Tidal Disruption Event AT 2019qiz. *Astrophys. J.* **917**, 9 (2021).
- [18] Patra, K. C. *et al.* Spectropolarimetry of the tidal disruption event AT 2019qiz: a quasi-spherical reprocessing layer. *Mon. Not. R. Astron. Soc.* **515**, 138–145 (2022).
- [19] Mummery, A. *et al.* Fundamental scaling relationships revealed in the optical light curves of tidal disruption events. *Mon. Not. R. Astron. Soc.* **527**, 2452–2489 (2024).

- [20] van Velzen, S. *et al.* Late-time UV Observations of Tidal Disruption Flares Reveal Unobserved, Compact Accretion Disks. *Astrophys. J.* **878**, 82 (2019).
- [21] Short, P. *et al.* Delayed appearance and evolution of coronal lines in the TDE AT2019qiz. *Mon. Not. R. Astron. Soc.* **525**, 1568–1587 (2023).
- [22] Evans, P. A. *et al.* Monthly quasi-periodic eruptions from repeated stellar disruption by a massive black hole. *Nat. Astron.* **7**, 1368–1375 (2023).
- [23] Arcodia, R. *et al.* The complex time and energy evolution of quasi-periodic eruptions in eRO-QPE1. *Astron. Astrophys.* **662**, A49 (2022).
- [24] Arcodia, R. *et al.* Cosmic hide and seek: the volumetric rate of X-ray quasi-periodic eruptions. *arXiv e-prints* arXiv:2403.17059 (2024).
- [25] Mummery, A. & Balbus, S. A. The spectral evolution of disc dominated tidal disruption events. *Mon. Not. R. Astron. Soc.* **492**, 5655–5674 (2020).
- [26] Grzędzielski, M., Janiuk, A., Czerny, B. & Wu, Q. Modified viscosity in accretion disks. Application to Galactic black hole binaries, intermediate mass black holes, and active galactic nuclei. *Astron. Astrophys.* **603**, A110 (2017).
- [27] Tagawa, H. & Haiman, Z. Flares from stars crossing active galactic nucleus discs on low-inclination orbits. *Mon. Not. R. Astron. Soc.* **526**, 69–79 (2023).
- [28] Suková, P., Zajaček, M., Witzany, V. & Karas, V. Stellar Transits across a Magnetized Accretion Torus as a Mechanism for Plasmoid Ejection. *Astrophys. J.* **917**, 43 (2021).
- [29] Stone, N. & Loeb, A. Observing Lense-Thirring Precession in Tidal Disruption Flares. *Phys. Rev. Lett.* **108**, 061302 (2012).

- [30] Franchini, A. *et al.* Quasi-periodic eruptions from impacts between the secondary and a rigidly precessing accretion disc in an extreme mass-ratio inspiral system. *Astron. Astrophys.* **675**, A100 (2023).
- [31] Yao, P. Z., Quataert, E., Jiang, Y.-F., Lu, W. & White, C. J. Star-Disk Collisions: Implications for QPEs and Other Transients Near Supermassive Black Holes. *arXiv e-prints* arXiv:2407.14578 (2024).
- [32] Babak, S. *et al.* Science with the space-based interferometer LISA. V. Extreme mass-ratio inspirals. *Phys. Rev. D* **95**, 103012 (2017).
- [33] Sazonov, S. *et al.* First tidal disruption events discovered by SRG/eROSITA: X-ray/optical properties and X-ray luminosity function at $z < 0.6$. *Mon. Not. R. Astron. Soc.* **508**, 3820–3847 (2021).
- [34] Yao, Y. *et al.* Tidal Disruption Event Demographics with the Zwicky Transient Facility: Volumetric Rates, Luminosity Function, and Implications for the Local Black Hole Mass Function. *Astrophys. J. Lett.* **955**, L6 (2023).
- [35] Linial, I. & Metzger, B. D. Coupled Disk-Star Evolution in Galactic Nuclei and the Lifetimes of QPE Sources. *arXiv e-prints* arXiv:2404.12421 (2024).
- [36] Fruscione, A. *et al.* Silva, D. R. & Doxsey, R. E. (eds) *CIAO: Chandra’s data analysis system*. (eds Silva, D. R. & Doxsey, R. E.) *Observatory Operations: Strategies, Processes, and Systems*, Vol. 6270 of *Society of Photo-Optical Instrumentation Engineers (SPIE) Conference Series*, 62701V (2006).
- [37] Gregory, P. C. & Loredo, T. J. A New Method for the Detection of a Periodic Signal of Unknown Shape and Period. *Astrophys. J.* **398**, 146 (1992).

- [38] Buchner, J. *et al.* X-ray spectral modelling of the AGN obscuring region in the CDFS: Bayesian model selection and catalogue. *Astron. Astrophys.* **564**, A125 (2014).
- [39] Buchner, J. Collaborative Nested Sampling: Big Data versus Complex Physical Models. *Publ. Astron. Soc. Pac.* **131**, 108005 (2019).
- [40] Arnaud, K. A. Jacoby, G. H. & Barnes, J. (eds) *XSPEC: The First Ten Years*. (eds Jacoby, G. H. & Barnes, J.) *Astronomical Data Analysis Software and Systems V*, Vol. 101 of *Astronomical Society of the Pacific Conference Series*, 17 (1996).
- [41] Evans, P. A. *et al.* An online repository of Swift/XRT light curves of γ -ray bursts. *Astron. Astrophys.* **469**, 379–385 (2007).
- [42] Evans, P. A. *et al.* Methods and results of an automatic analysis of a complete sample of Swift-XRT observations of GRBs. *Mon. Not. R. Astron. Soc.* **397**, 1177–1201 (2009).
- [43] Mummery, A. Tidal disruption event discs are larger than they seem: removing systematic biases in TDE X-ray spectral modelling. *Mon. Not. R. Astron. Soc.* **507**, L24–L28 (2021).
- [44] Guolo, M. *et al.* A systematic analysis of the X-ray emission in optically selected tidal disruption events: observational evidence for the unification of the optically and X-ray selected populations. *arXiv e-prints* arXiv:2308.13019 (2023).
- [45] Gendreau, K. C., Arzoumanian, Z. & Okajima, T. Takahashi, T., Murray, S. S. & den Herder, J.-W. A. (eds) *The Neutron star Interior Composition ExploreR (NICER): an Explorer mission of opportunity for soft x-ray timing spectroscopy*. (eds Takahashi, T., Murray, S. S. & den Herder, J.-W. A.) *Space Telescopes and Instrumentation 2012: Ultraviolet to Gamma Ray*, Vol. 8443 of *Society of Photo-Optical Instrumentation Engineers (SPIE) Conference Series*, 844313 (2012).

- [46] Arzoumanian, Z. *et al.* Takahashi, T., den Herder, J.-W. A. & Bautz, M. (eds) *The neutron star interior composition explorer (NICER): mission definition.* (eds Takahashi, T., den Herder, J.-W. A. & Bautz, M.) *Space Telescopes and Instrumentation 2014: Ultraviolet to Gamma Ray*, Vol. 9144 of *Society of Photo-Optical Instrumentation Engineers (SPIE) Conference Series*, 914420 (2014).
- [47] HI4PI Collaboration *et al.* HI4PI: A full-sky H I survey based on EBHIS and GASS. *Astron. Astrophys.* **594**, A116 (2016).
- [48] Singh, K. P. *et al.* Takahashi, T., den Herder, J.-W. A. & Bautz, M. (eds) *ASTROSAT mission.* (eds Takahashi, T., den Herder, J.-W. A. & Bautz, M.) *Space Telescopes and Instrumentation 2014: Ultraviolet to Gamma Ray*, Vol. 9144 of *Society of Photo-Optical Instrumentation Engineers (SPIE) Conference Series*, 91441S (2014).
- [49] Singh, K. P. *et al.* Soft X-ray Focusing Telescope Aboard AstroSat: Design, Characteristics and Performance. *Journal of Astrophysics and Astronomy* **38**, 29 (2017).
- [50] Tandon, S. N. *et al.* In-orbit Calibrations of the Ultraviolet Imaging Telescope. *Astron. J.* **154**, 128 (2017).
- [51] Tandon, S. N. *et al.* Additional Calibration of the Ultraviolet Imaging Telescope on Board AstroSat. *Astron. J.* **159**, 158 (2020).
- [52] Antonini, F. Origin and Growth of Nuclear Star Clusters around Massive Black Holes. *Astrophys. J.* **763**, 62 (2013).
- [53] Turner, M. L. *et al.* The ACS Fornax Cluster Survey. VI. The Nuclei of Early-type Galaxies in the Fornax Cluster. *Astrophys. J. Suppl. Ser.* **203**, 5 (2012).
- [54] Patra, K. C. *et al.* Constraints on the narrow-line region of the X-ray quasi-periodic eruption source GSN 069. *arXiv e-prints* arXiv:2310.05574 (2023).

- [55] Bellm, E. C. *et al.* The Zwicky Transient Facility: System Overview, Performance, and First Results. *Publ. Astron. Soc. Pac.* **131**, 018002 (2019).
- [56] van Velzen, S. *et al.* Seventeen Tidal Disruption Events from the First Half of ZTF Survey Observations: Entering a New Era of Population Studies. *Astrophys. J.* **908**, 4 (2021).
- [57] Tonry, J. L. *et al.* ATLAS: A High-cadence All-sky Survey System. *Publ. Astron. Soc. Pac.* **130**, 064505 (2018).
- [58] Chambers, K. C. *et al.* The Pan-STARRS1 Surveys. *arXiv e-prints* arXiv:1612.05560 (2016).
- [59] Fabricius, C. *et al.* Gaia Data Release 1. Pre-processing and source list creation. *Astron. Astrophys.* **595**, A3 (2016).
- [60] Magnier, E. A. *et al.* The Pan-STARRS Data-processing System. *Astrophys. J. Suppl. Ser.* **251**, 3 (2020).
- [61] Magnier, E. A. *et al.* Pan-STARRS Pixel Analysis: Source Detection and Characterization. *Astrophys. J. Suppl. Ser.* **251**, 5 (2020).
- [62] Waters, C. Z. *et al.* Pan-STARRS Pixel Processing: Detrending, Warping, Stacking. *Astrophys. J. Suppl. Ser.* **251**, 4 (2020).
- [63] Masci, F. J. *et al.* A New Forced Photometry Service for the Zwicky Transient Facility. *arXiv e-prints* arXiv:2305.16279 (2023).
- [64] Steele, I. A. *et al.* Oschmann, J., Jacobus M. (ed.) *The Liverpool Telescope: performance and first results.* (ed. Oschmann, J., Jacobus M.) *Ground-based Telescopes*, Vol. 5489 of *Society of Photo-Optical Instrumentation Engineers (SPIE) Conference Series*, 679–692 (2004).

- [65] Dhillon, V. S. *et al.* ULTRACAM: an ultrafast, triple-beam CCD camera for high-speed astrophysics. *Mon. Not. R. Astron. Soc.* **378**, 825–840 (2007).
- [66] Dhillon, V. S. *et al.* HiPERCAM: a quintuple-beam, high-speed optical imager on the 10.4-m Gran Telescopio Canarias. *Mon. Not. R. Astron. Soc.* **507**, 350–366 (2021).
- [67] Nicholl, M. *et al.* AT 2022aedm and a New Class of Luminous, Fast-cooling Transients in Elliptical Galaxies. *Astrophys. J. Lett.* **954**, L28 (2023).
- [68] Johnson, B. D., Leja, J., Conroy, C. & Speagle, J. S. Stellar Population Inference with Prospector. *Astrophys. J. Suppl. Ser.* **254**, 22 (2021).
- [69] Schlafly, E. F. & Finkbeiner, D. P. Measuring Reddening with Sloan Digital Sky Survey Stellar Spectra and Recalibrating SFD. *Astrophys. J.* **737**, 103 (2011).
- [70] Postma, J. E. & Leahy, D. CCDLAB: A Graphical User Interface FITS Image Data Reducer, Viewer, and Canadian UVIT Data Pipeline. *Publ. Astron. Soc. Pac.* **129**, 115002 (2017).
- [71] Mummery, A. & Turner, S. G. D. The turbulent variability of accretion discs observed at high energies. *Mon. Not. R. Astron. Soc.* (2024).
- [72] Dai, L., McKinney, J. C., Roth, N., Ramirez-Ruiz, E. & Miller, M. C. A Unified Model for Tidal Disruption Events. *Astrophys. J. Lett.* **859**, L20 (2018).
- [73] Shiokawa, H., Krolik, J. H., Cheng, R. M., Piran, T. & Noble, S. C. General Relativistic Hydrodynamic Simulation of Accretion Flow from a Stellar Tidal Disruption. *Astrophys. J.* **804**, 85 (2015).
- [74] Foreman-Mackey, D., Hogg, D. W., Lang, D. & Goodman, J. emcee: The MCMC Hammer. *Publ. Astron. Soc. Pac.* **125**, 306 (2013).

- [75] Mummery, A. Asymptotic Green’s function solutions of the general relativistic thin disc equations. *Mon. Not. R. Astron. Soc.* **518**, 1905–1916 (2023).
- [76] Done, C., Davis, S. W., Jin, C., Blaes, O. & Ward, M. Intrinsic disc emission and the soft X-ray excess in active galactic nuclei. *Mon. Not. R. Astron. Soc.* **420**, 1848–1860 (2012).
- [77] Salvesen, G. & Miller, J. M. Black hole spin in X-ray binaries: giving uncertainties an f. *Mon. Not. R. Astron. Soc.* **500**, 3640–3666 (2021).
- [78] Chakraborty, J. *et al.* Testing EMRI Models for Quasi-periodic Eruptions with 3.5 yr of Monitoring eRO-QPE1. *Astrophys. J.* **965**, 12 (2024).
- [79] Franchini, A., Lodato, G. & Facchini, S. Lense-Thirring precession around supermassive black holes during tidal disruption events. *Mon. Not. R. Astron. Soc.* **455**, 1946–1956 (2016).
- [80] Raj, A. & Nixon, C. J. Disk Tearing: Implications for Black Hole Accretion and AGN Variability. *Astrophys. J.* **909**, 82 (2021).
- [81] Pasham, D. R. *et al.* Lense-Thirring Precession after a Supermassive Black Hole Disrupts a Star. *arXiv e-prints* arXiv:2402.09689 (2024).
- [82] Ingram, A., Motta, S. E., Aigrain, S. & Karastergiou, A. A self-lensing binary massive black hole interpretation of quasi-periodic eruptions. *Mon. Not. R. Astron. Soc.* **503**, 1703–1716 (2021).
- [83] Cannizzo, J. K. The Accretion Disk Limit Cycle Model: Toward an Understanding of the Long-Term Behavior of SS Cygni. *Astrophys. J.* **419**, 318 (1993).
- [84] King, A. GSN 069 - A tidal disruption near miss. *Mon. Not. R. Astron. Soc.* **493**, L120–L123 (2020).

- [85] Krolik, J. H. & Linial, I. Quasiperiodic Erupters: A Stellar Mass-transfer Model for the Radiation. *Astrophys. J.* **941**, 24 (2022).
- [86] Lu, W. & Quataert, E. Quasi-periodic eruptions from mildly eccentric unstable mass transfer in galactic nuclei. *Mon. Not. R. Astron. Soc.* **524**, 6247–6266 (2023).
- [87] Wevers, T. *et al.* An elliptical accretion disk following the tidal disruption event AT 2020zso. *Astron. Astrophys.* **666**, A6 (2022).
- [88] Holoien, T. W. S. *et al.* PS18kh: A New Tidal Disruption Event with a Non-axisymmetric Accretion Disk. *Astrophys. J.* **880**, 120 (2019).
- [89] Short, P. *et al.* The tidal disruption event AT 2018hyz - I. Double-peaked emission lines and a flat Balmer decrement. *Mon. Not. R. Astron. Soc.* **498**, 4119–4133 (2020).
- [90] Hung, T. *et al.* Double-peaked Balmer Emission Indicating Prompt Accretion Disk Formation in an X-Ray Faint Tidal Disruption Event. *Astrophys. J.* **903**, 31 (2020).
- [91] Andalman, Z. L., Liska, M. T. P., Tchekhovskoy, A., Coughlin, E. R. & Stone, N. Tidal disruption discs formed and fed by stream-stream and stream-disc interactions in global GRHD simulations. *Mon. Not. R. Astron. Soc.* **510**, 1627–1648 (2022).
- [92] Bonnerot, C. & Lu, W. Simulating disc formation in tidal disruption events. *Mon. Not. R. Astron. Soc.* **495**, 1374–1391 (2020).
- [93] Curd, B. Global simulations of tidal disruption event disc formation via stream injection in GRRMHD. *Mon. Not. R. Astron. Soc.* **507**, 3207–3227 (2021).
- [94] Kormendy, J. & Ho, L. C. Coevolution (Or Not) of Supermassive Black Holes and Host Galaxies. *Annu. Rev. Astron. Astrophys.* **51**, 511–653 (2013).

- [95] Gültekin, K. *et al.* The M- σ and M-L Relations in Galactic Bulges, and Determinations of Their Intrinsic Scatter. *Astrophys. J.* **698**, 198–221 (2009).
- [96] McConnell, N. J. & Ma, C.-P. Revisiting the Scaling Relations of Black Hole Masses and Host Galaxy Properties. *Astrophys. J.* **764**, 184 (2013).
- [97] Guillochon, J. *et al.* MOSFiT: Modular Open Source Fitter for Transients. *Astrophys. J. Suppl. Ser.* **236**, 6 (2018).
- [98] Mockler, B., Guillochon, J. & Ramirez-Ruiz, E. Weighing Black Holes Using Tidal Disruption Events. *Astrophys. J.* **872**, 151 (2019).
- [99] Nicholl, M. *et al.* Systematic light-curve modelling of TDEs: statistical differences between the spectroscopic classes. *Mon. Not. R. Astron. Soc.* **515**, 5604–5616 (2022).
- [100] Ryu, T., Krolik, J. & Piran, T. Measuring Stellar and Black Hole Masses of Tidal Disruption Events. *Astrophys. J.* **904**, 73 (2020).

Data Availability: All *NICER*, *Chandra* and *Swift* data presented here are public and can be found in the NASA archives at the following URL: <https://heasarc.gsfc.nasa.gov/cgi-bin/W3Browse/w3browse.pl>. *HST* data are public via the MAST archive: <https://archive.stsci.edu/missions-and-data/hst>. The reduced light curve data from Figs. 1 and 4 are available via this repository: <https://github.com/mnicholl/AT2019qiz>.

Code Availability: Data reduction and X-ray spectral fitting were performed using standard publicly available codes (Methods). Code used for the relativistic disk model is described by Refs. [25, 19]. Author AM is working towards releasing a user-friendly version of this code publicly via GitHub; the current version will be shared on request.

Acknowledgments: We thank two anonymous referees for their insightful and helpful comments. We thank the Swift, AstroSat and NICER teams for scheduling our DDT requests. We thank the participants of the Kavli Institute for Theoretical Physics ‘TDE24’ meeting and Chris Done for helpful discussions. MN, AA, CA and XS are supported by the European Research Council (ERC) under the European Union’s Horizon 2020 research and innovation programme (grant agreement No. 948381) and by UK Space Agency Grant No. ST/Y000692/1. DRP was funded by NASA grant 80NSSC19K1287. This work was supported by a Leverhulme Trust International Professorship grant [number LIP-202-014]. ECF is supported by NASA under award number 80GSFC21M0002. AH is supported by Carlsberg Foundation Fellowship Programme 2015. VSD and ULTRACAM are funded by the Science and Technology Facilities Council (grant ST/Z000033/1). AJ is supported by grant No. 2023/50/A/ST9/00527 from the Polish National Science Center. EJR and PR are supported by Science and Technology Facilities Council (STFC) studentships. KDA acknowledges support from the National Science Foundation through award AST-2307668. KA is supported by the Australian Research Council

Discovery Early Career Researcher Award (DECRA) through project number DE230101069. TWC acknowledges the Yushan Young Fellow Program by the Ministry of Education, Taiwan for the financial support. RC benefitted from interactions with Theory Network participants that were funded by the Gordon and Betty Moore Foundation through Grant GBMF5076. KCP is funded in part by generous support from Sunil Nagaraj, Landon Noll and Sandy Otellini. EN acknowledges support from NASA theory grant 80NSSC20K0540. AI acknowledges support from the Royal Society. SGDT acknowledges support under STFC Grant ST/X001113/1. AFG acknowledges support from the Department for the Economy (DfE) Northern Ireland postgraduate studentship scheme. This research was supported in part by grant NSF PHY-2309135 to the Kavli Institute for Theoretical Physics (KITP). This research has made use of data obtained from the Chandra Data Archive and the Chandra Source Catalog, and software provided by the Chandra X-ray Center (CXC) in the application packages CIAO and Sherpa. The AstroSat mission is operated by the Indian Space Research Organisation (ISRO), the data are archived at the Indian Space Science Data Centre (ISSDC). The SXT data-processing software is provided by the Tata Institute of Fundamental Research (TIFR), Mumbai, India. The UVIT data were checked and verified by the UVIT POC at IIA, Bangalore, India. We acknowledge the use of public data from the Swift data archive. The Pan-STARRS telescopes are supported by NASA Grants NNX12AR65G and NNX14AM74G. ZTF is supported by the National Science Foundation under Grants No. AST-1440341 and AST-2034437 and a collaboration including current partners Caltech, IPAC, the Oskar Klein Center at Stockholm University, the University of Maryland, University of California, Berkeley, the University of Wisconsin at Milwaukee, University of Warwick, Ruhr University, Cornell University, Northwestern University and Drexel University. Operations are conducted by COO, IPAC, and UW. The Liverpool Telescope is operated on the island of La Palma by Liverpool John Moores University in the Spanish Observatorio del Roque de los Muchachos of the Instituto de Astrofísica de Canarias with financial support from the UK Science and Technology Facilities Council.

Author contributions: MN was PI of the *Chandra*, *HST*, *Swift* and LT programs, performed data analysis, and led the writing and overall project. DRP triggered the *NICER* and *AstroSat* follow-up, performed X-ray data reduction and analysis, and wrote parts of the manuscript. AM performed the accretion disk modeling and wrote parts of the manuscript. MG performed X-ray data reduction and spectral analysis, the comparison to other QPE sources, and wrote parts of the manuscript. KG and ECF coordinated the *NICER* observations. KG is the PI of *NICER*. GCW coordinated *AstroSat* observations and reduced the data. RR performed *NICER* data reduction. CB and JC contributed to the precession analysis. AH performed *Chandra* data reduction. VSD organised and reduced the ULTRACAM observations. AFG analysed the *HST* PSF. JG analysed the Pan-STARRS plateau. MEH obtained the Pan-STARRS observations. AJ contributed to pressure instability models. GS analysed the SMBH spin systematics. SvV contributed the ZTF forced photometry. AA, KDA, KA, EB, YC, RC, SG, BPG, TL, AL, RM, SLM, SRO, EJR, XS contributed to the *Chandra +HST* program. ZA, ACF, ECF, KG, EK, RR are members of the *NICER* team. ZA and KG carried out the *NICER* observations. AA, CRA, TWC, MDF, JHG, TM, PR, XS, SJS, KWS, SS, HFS, JW, DRY are members of the Pan-STARRS transients team. TdB, KCC, HG, JH, CCL, TBL, EAM, PM, SJS, KWS, RJW, DRY contribute to the operation of Pan-STARRS. AI, EN, SGDT provided theoretical expertise. RC, RM, KCP, VR, RS are members of the ZTF TDE group. TW provided *HST* expertise. All authors provided feedback on the manuscript.

Competing interests: The authors declare that there are no competing interests.

Additional information: Correspondence and requests for materials should be addressed to Matt Nicholl (matt.nicholl@qub.ac.uk).